
Cross-modal Transfer Through Time for Sensor-based Human Activity Recognition

Abhi Kamboj¹Anh Duy Nguyen¹Minh N. Do¹

University of Illinois at Urbana-Champaign¹
 {akamboj2, duyuan2, minhdo}@illinois.edu

Abstract

In order to unlock the potential of diverse sensors, we investigate a method to transfer knowledge between time-series modalities using a multimodal *temporal* representation space for Human Activity Recognition (HAR). Specifically, we explore the setting where the modality used in testing has no labeled data during training, which we refer to as Unsupervised Modality Adaptation (UMA). We categorize existing UMA approaches as Student-Teacher or Contrastive Alignment methods. These methods typically compress continuous-time data samples into single latent vectors during alignment, inhibiting their ability to transfer temporal information through real-world temporal distortions. To address this, we introduce Cross-modal Transfer Through Time (C3T), which preserves temporal information during alignment to handle dynamic sensor data better. C3T achieves this by aligning a set of temporal latent vectors across sensing modalities. Our extensive experiments on various camera+IMU datasets demonstrate that C3T outperforms existing methods in UMA by at least 8% in accuracy and shows superior robustness to temporal distortions such as time-shift, misalignment, and dilation. Our findings suggest that C3T has significant potential for developing generalizable models for time-series sensor data, opening new avenues for various multimodal applications.

1 Introduction

Human activity recognition (HAR) across different sensing modalities remains a significant challenge in machine learning, particularly when adapting to new sensors without labeled data. A limitation of existing cross-modal feature alignment methods is that they compress an entire time-series sequence into a single latent vector, hindering the transfer of temporal information [1–3]. This compression is especially problematic when training and testing on real-world continuous sensor data, such as wearable inertial data, where the same action may occur with significant temporal variations (different speeds, starting points, or durations). We introduce Cross-modal Transfer Through Time (C3T), a novel approach that preserves fine-grained temporal information during cross-modal alignment, enabling more effective knowledge transfer. C3T outperforms conventional contrastive alignment approaches and demonstrates robustness to common temporal distortions in our experiments performing cross-modal transfer from RGB videos to inertial sensors.

Inertial Measurement Units (IMUs), which typically provide 3-axis acceleration and 3-axis gyroscopic information on a wearable device, emerge as strong candidates for understanding human motion in a nonintrusive fashion. Smartwatches, smartphones, earbuds, and other wearables have enabled the seamless integration of IMUs into daily life [4]. Unfortunately, IMUs remain underutilized in current machine-learning approaches due to several challenges, including: (1) the scarcity of labeled IMU data stemming from the difficulty in interpreting raw sensor readings, and (2) the challenge of defining precise activity boundaries given the continuous time-series nature of IMU data.

lack the generalization capability seen in visual and textual models, which benefit from Internet-scale data. Beyond IMUs, various sensing modalities are gaining popularity in wearables (e.g., surface electrocardiogram, electromyography) and ambient monitoring systems (e.g., WiFi signals, Radar). Researchers have developed numerous AI methods for HAR using these modalities; however, these methods As new sensing modalities emerge, a critical challenge is *how to effectively transfer knowledge from data-rich modalities to new sensor types without requiring extensive labeling effort*.

A promising solution is cross-modal transfer, where knowledge from a well-labeled source modality is transferred to an unlabeled target modality [5]. However, current cross-modality and missing-modality techniques are semi-supervised with some labeled examples from each modality during training [6–11]. This creates a significant barrier to adopting new sensing technologies, as each application would require costly re-labeling efforts, and inhibits real-time unsupervised transfer as described in Figure 1. To address these practical challenges, we explore a setting where the target modality is completely unlabeled during training. We refer to this as *Unsupervised Modality Adaptation* (UMA), akin to Unsupervised Domain Adaptation where the domain is a new modality [12, 13].

Currently, two approaches can address UMA:

1. Student-Teacher (ST) methods: These leverage a teacher modality to distill knowledge to the student modality, a technique commonly used for domain adaptation and semi-supervised learning [14–16, 9, 17].
2. Contrastive Alignment (CA): This approach aligns latent representations of data samples across modalities and employs a shared task head for cross-modal transfer [1–3].

Further motivation for the term UMA, and review of existing ST and CA methods for RGB to IMU transfer is provided in the Related Works (Section 7.1).

Although these methods work well for image and text modalities, when applied to sensor signals, they compress an entire time-series sequence into a single latent representation for alignment. This approach does not account for the continuous nature of real-world data and the variable time spans over which actions occur. The proposed method, Cross-modal Transfer Through Time (C3T), (1) extracts a time-varying latent dimension through the feature maps outputted from temporal convolutions, (2) performs contrastive alignment across modalities in this temporal latent space, and (3) uses a shared self-attention head to perform the transfer. **C3T aligns local temporal features across modalities at a fine-grained level, avoiding the loss of complex temporal dependencies during transfer.**

Our research evaluates these three UMA methods—ST, CA, and C3T—focusing on knowledge transfer from RGB videos to IMU signals across four diverse HAR datasets. C3T outperforms existing methods by at least 8% in top-1 accuracy on all datasets. Additional experiments demonstrate C3T’s superior resilience to time-shift, misalignment, and time-dilation noise. This is particularly valuable for real-world continuous human activity recognition, where the start and the end of an activity are not well defined, and actions can occur at various speeds.

Furthermore, a qualitative analysis of the multi-modal representation space reveals that contrastive methods excel by uncovering latent correlations between modalities, enabling cross-modal information transfer without labeled data. Additional visualizations of C3T’s attention weights demonstrate how temporal shifts are captured across the temporal latent vectors, suggesting its performance gain stems from its robustness to temporal dynamics.

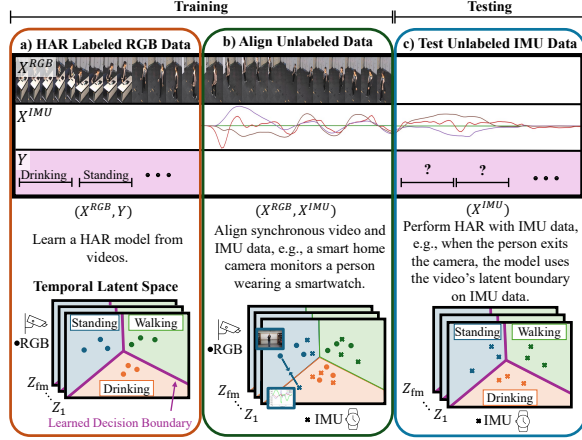


Figure 1: **Motivation for Unsupervised Modality Adaptation:** Depicts a scenario in which an AI system can perform inference on a new modality without additional annotation effort, through latent space alignment with a pretrained modality. C3T leverages a temporal latent space for more robust transfer.

The promising results of C3T open new avenues for developing highly generalizable models for time-series sensor data. This has implications across various domains, including healthcare monitoring, smart homes, industrial IoT, and human-computer interaction, where multi-modal learning from limited labeled sensor data is crucial [13]. **Our novel contributions are as follows:**

- A formulation of the Unsupervised Modality Adaptation (UMA) setting for Human Activity Recognition (HAR), with a categorization of existing methods into Student-Teacher (ST) and Contrastive Alignment (CA) approaches. We introduce Cross-modal Transfer Through Time (C3T), and a corresponding temporal alignment loss function \mathcal{L}_{C3T} (Section 7.1 to Section 3).
- A comprehensive evaluation and comparison of ST, CA, and C3T methods in the UMA setting on clean data and with temporal noise. These experiments demonstrate C3T’s superior performance and robustness (Section 4).
- An in-depth examination of cross-modal alignment and C3T’s structure, including visualizations of the multimodal representation space, a comparison of model sizes, and additional experiments on training and testing methods. This examination reveals insights into effective cross-modal transfer and its potential real-world applications for sensor data (Section 4 and Section 5).

2 Background

We investigate the creation of a robust multimodal latent space for human action recognition, denoted as \mathcal{Z} , that can be leveraged for UMA. In this context, robustness refers to the ability of the latent space to maintain consistent representations despite shifts in input distribution to different modalities or temporal noise. We assume that there exists a learnable projection $f^{(k)}$ from every modality $k \in 1, \dots, M$ to this latent space \mathcal{Z} , i.e., $f^{(k)} : \mathcal{X}^{(k)} \rightarrow \mathcal{Z}$, such that the same actions viewed from different modalities map to proximal points in \mathcal{Z} , while distinct actions map to disparate regions. We further assume there exists a learnable mapping h from the latent space \mathcal{Z} to the label space of human actions \mathcal{Y} , i.e., $h : \mathcal{Z} \rightarrow \mathcal{Y}$. This mapping should be invariant to the originating modality of the latent representation. Our method leverages the intuition that proximity in the latent space \mathcal{Z} indicates semantic similarity, i.e. neighboring points are likely map to the same class regardless of their originating modality. We use cosine similarity to measure *nearness*, as it’s more effective in high-dimensional spaces than Euclidean distance [18]. This choice focuses on directional similarity, mitigates the curse of dimensionality, and aligns with the distributional hypothesis in representation learning.

For simplicity, we experiment with two modalities, $M = 2$, and assume that a dataset of n data points is split into four disjoint index sets $I_1 \cup I_2 \cup I_3 \cup I_4 \in \{1 \dots n\}$. Under our UMA setting, during training, the model has access to two of these sub-datasets. One contains labeled data for one modality, $\mathcal{D}_{\text{HAR}} = \{(\mathbf{x}_i^{(1)}, \mathbf{y}_i)\}_{i=1}^{I_1}$, and the other contains synchronous data between the modalities, but these points are unlabeled, $\mathcal{D}_{\text{Align}} = \{(\mathbf{x}_i^{(1)}, \mathbf{x}_i^{(2)})\}_{i=1}^{I_2}$. This is analogous to having an existing sensor with labeled data and introducing a new sensor in which data can be synchronously collected, but there is no additional annotation effort (Figure 1). The third and fourth sets are used for validation and testing and contain only labeled data from the second modality, i.e. $\mathcal{D}_{\text{Val}} = \{(\mathbf{x}_i^{(2)}, \mathbf{y}_i)\}_{i=1}^{I_3}$ and $\mathcal{D}_{\text{Test}} = \{(\mathbf{x}_i^{(2)}, \mathbf{y}_i)\}_{i=1}^{I_4}$.

3 Unsupervised Modality Adaptation Methods

In this section, we formulate and compare the Student-teacher, Contrastive Alignment and Cross-modal Transfer Through Time approaches. In the context of human action or activity recognition (HAR), we conduct experiments using RGB videos as the source domain, $x^{(1)} = x^{(\text{RGB})}$, and Inertial Measurement Unit (IMU) data as the target $x^{(2)} = x^{(\text{IMU})}$. As depicted for each method in Figure 2, training for UMA occurs in two phases: a) Supervised Learning with RGB data on \mathcal{D}_{HAR} and b) Unsupervised alignment across both modalities on $\mathcal{D}_{\text{Align}}$. Inference (phase c) occurs on IMU data on \mathcal{D}_{Val} or $\mathcal{D}_{\text{Test}}$.

Student-Teacher: We adopt a student-teacher (ST) method similar to Thoker and Gall [14] for UMA. ST leverages the teacher RGB video model trained in *phase a* to produce pseudo-labels to train the student IMU model in *phase b* of Figure 2. In this case, the latent transfer space is the output logit space, $\mathcal{Z} = \mathcal{Y}$, or equivalently the HAR module is the identity $h = \mathbb{1}$, and the cross-modal

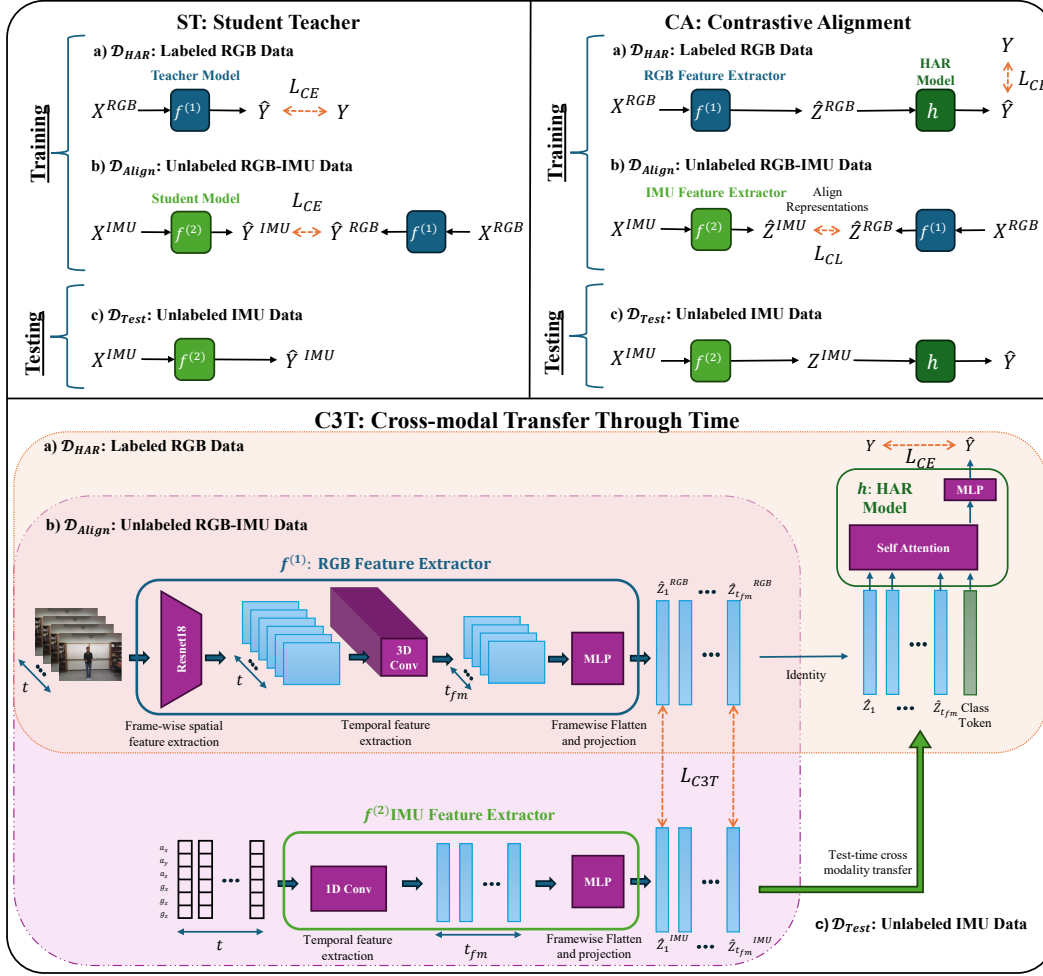


Figure 2: **Unsupervised Modality Adaptation Methods:** Training happens in two phases: a) trains the HAR model on labeled RGB inputs and b) aligns unlabeled IMU and RGB modalities. UMA testing c) occurs on unlabeled IMU data.

representations are aligned using the standard cross-entropy loss \mathcal{L}_{CE} (Appendix Equation (3)). We denote the teacher network as $f^{(1)} : \mathcal{X}^{(1)} \rightarrow \mathcal{Y}$ and the student network as $f^{(2)} : \mathcal{X}^{(2)} \rightarrow \mathcal{Y}$. First, we train the teacher $f^{(1)}$ on \mathcal{D}_{HAR} with labeled RGB data. Next, since \mathcal{D}_{Align} does not contain labels, we use $f^{(1)}(x_i^{(1)}) = \hat{y}_i^{(1)}$ to generate pseudo-labels for every datapoint $i \in I_2$. Then we use the augmented dataset $\hat{\mathcal{D}}_{Align} = \{(\mathbf{x}_i^1, \mathbf{x}_i^2, \hat{\mathbf{y}}_i^{(1)})\}_{i=1}^{I_2}$ to train $f^{(2)}$. The teacher network minimizes $\mathcal{L}_{CE}(P_{f^{(1)}(x)}, P_y)$ and the student minimizes $\mathcal{L}_{CE}(P_{f^{(2)}(x)}, P_{\hat{y}_i^{(1)}})$, where P represents the distribution generated by the labels, pseudo-labels or an encoder’s output logits.

Contrastive Alignment: We adopt the contrastive alignment (CA) method from past works [1–3] for our UMA setting. In our work, CA performs *phase a* similar to ST; however, it trains a model with two parts: An encoder $f^{(1)}$ to extract the latent variable z , and a task-specific MLP head h . The extracted latent space \mathcal{Z} enables scalability and interoperability for adding different sensing modalities, types of encoders, and output task heads.

In *phase b* of training, CA performs unsupervised contrastive alignment with the outputs of the RGB encoder $f^{(1)}$ and the IMU encoder $f^{(2)}$ on unlabeled data. To align different modalities in the feature space on \mathcal{D}_{Align} we use a symmetric contrastive loss formulation \mathcal{L}_{CL} [18, 1–3] with temperature parameter τ and batch size B :

$$\mathcal{L}_{CL} = -\frac{1}{B} \sum_{i=1}^B \log \frac{\exp(\langle \hat{z}_i^{(1)}, \hat{z}_i^{(2)} \rangle / \tau)}{\sum_{j=1}^B \exp(\langle \hat{z}_i^{(1)}, \hat{z}_j^{(2)} \rangle / \tau)}, \text{ where } \hat{z}_i^{(k)} = \frac{f^{(k)}(x_i^{(k)})}{\|f^{(k)}(x_i^{(k)})\|}, k \in \{1, 2\}. \quad (1)$$

Table 1: **UMA vs. Supervised Performance:** The supervised baselines trains on \mathcal{D}_{HAR} , using labels for both modalities. The Unsupervised Modality Adaptation (UMA) methods train with labeled RGB data in \mathcal{D}_{HAR} and unlabeled RGB+IMU data on $\mathcal{D}_{\text{Align}}$ as described in Figures 1 and 2. The Top-1 and Top-3 accuracies on $\mathcal{D}_{\text{Test}}$ are shown. C3T outperforms the other UMA methods and nears the performance of the supervised setting, in four diverse datasets capturing various scenes, occlusions, IMU placements, and camera views.

	Model	UTD-MHAD [19]		CZU-MHAD [20]		MMACT [16]		MMEA-CL [21]	
		Top-1	Top-3	Top-1	Top-3	Top-1	Top-3	Top-1	Top-3
Supervised	IMU	87.9	97.7	95.1	98.2	70.0	90.0	65.8	87.6
	RGB	53.8	73.1	94.0	99.7	42.1	61.6	54.2	77.1
	Fusion	62.5	82.2	95.0	98.5	76.7	92.0	80.1	92.7
UMA	Random	3.7	11.1	4.6	16.6	2.9	8.6	3.1	9.4
	ST [14]	12.9	24.6	41.1	61.9	17.6	34.7	9.9	22.7
	CA [3]	42.6	67.4	70.0	92.7	24.5	47.6	29.3	51.7
	C3T (Ours)	62.5	86.4	84.2	96.7	32.4	57.9	51.2	78.8

Equation (1) clusters representations in \mathcal{Z} by cosine similarity, which brings about the desired property of the latent space that semantically similar vectors are proximal.

Cross-modal Transfer Through Time: CA and ST do not leverage latent temporal information as they collapse the entire time sequence into one latent vector. We thus propose a Cross-modal Transfer Through Time (C3T) model that leverages the temporal information of time-series sensors when aligning their representations. For a given time series input $x_{i,t}^{(k)}$ for sample i in a dataset, timestep $t = 1 \dots T$ of modality k , C3T leverages an encoder $f^{(k)} : \mathcal{X}_T^{(k)} \rightarrow \mathcal{Z}_{t_{\text{fm}}}$ to extract a set of t_{fm} latent vectors, z_t , from the feature map of temporal convolutions. Thus, the number of latent vectors is the length of the temporal dimension after convolution given by $t_{\text{fm}} = \left\lfloor \frac{T+2P-D(K-1)-1}{S} + 1 \right\rfloor$ where P, D, K, and S are the padding, dilation, kernel size, and stride, respectively.

Furthermore, during the alignment phase, C3T aligns each of these latent time vectors with the same time vector from the other modality. The new loss function extends the contrastive loss formulation to compare every time step t for the same data sample to all the other data samples and their time steps in the batch. Thus for a batch of size B with the data for every time step t , element i and modality k being indicated by $x_{i,t}^{(k)}$, \mathcal{L}_{C3T} can be calculated as follows:

$$\mathcal{L}_{\text{C3T}} = -\frac{1}{B} \sum_{i=1}^B \sum_{t=1}^{t_{\text{fm}}} \log \frac{\exp(\langle \hat{z}_{i,t}^{(1)}, \hat{z}_{i,t}^{(2)} \rangle / \tau)}{\sum_{j=1}^B \sum_{t=1}^{t_{\text{fm}}} \exp(\langle \hat{z}_{i,t}^{(1)}, \hat{z}_{j,t}^{(2)} \rangle / \tau)}, \text{ where } \hat{z}_{i,t}^{(k)} = \frac{f^{(k)}(x_{i,t}^{(k)})}{\|f^{(k)}(x_{i,t}^{(k)})\|}, k \in \{1, 2\} \quad (2)$$

C3T enables the use of a self-attention HAR module to extract global temporal features after the alignment of local temporal features across modalities, as shown in Figure 2. C3T’s HAR self-attention head, h , utilizes a class token similar to ViT [22], with temporal feature map vectors serving as input in place of image patches.

4 Unsupervised Modality Adaptation and Temporal Noise Experiments

Implementation: Our experiments utilize three key neural network modules:

1. *Video Feature Encoder $f^{(1)}$:* We employ a pretrained ResNet18 on every frame of the video followed by 3D convolution and a 2-layer multi-layer perceptron (MLP) with ReLU activations. Resnet is a well-established lightweight spatial feature extractor [23], and 3D convolutions are an effective temporal feature extractor [24, 25].
2. *IMU Feature Encoder $f^{(2)}$:* A 1D CNN followed by an MLP is used here. CNNs have shown superior performance in extracting features from time-series data like IMU signals, efficiently capturing local patterns and temporal dependencies [26].
3. *HAR Task Decoder h :* ST does not require h and CA uses an MLP. C3T employs a self-attention module to better capture long-range dependencies in the latent space, which is particularly beneficial for complex action sequences [27].

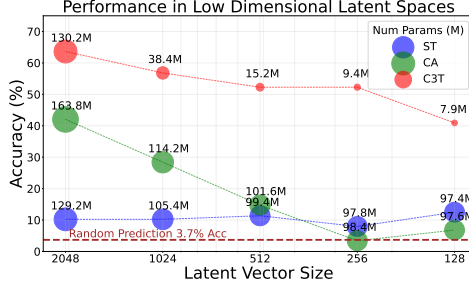


Figure 3: **Accuracy vs Latent Size:** Accuracy decreases with latent vector size. C3T maintains superior performance in scaling to smaller models.

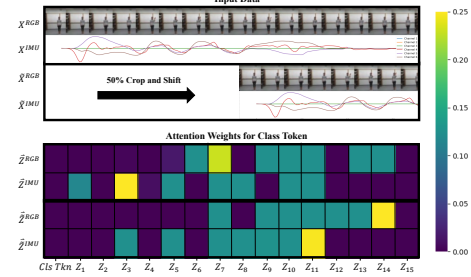


Figure 4: **Attention heatmap for C3T's HAR module:** Input shifts shift the attention weights of the temporal latent vectors.

Table 2: **Noise Experiments:** Performance of ST, CA, and C3T under various noise conditions. All results report UMA accuracy and its **percent difference** from the Original (no noise) column.

Model	Original	1. Crop	2. Misalign	3. Dilate	4. All
ST [14]	12.9	3.4 (-73.6%)	5.7 (-55.8%)	5.7 (-55.8%)	10.2 (-20.9%)
CA [3]	42.6	10.2 (-76.1%)	2.3 (-94.6%)	21.6 (-49.3%)	18.2 (-57.3%)
C3T	62.5	52.3 (-16.3%)	46.6 (-25.4%)	56.8 (-9.1%)	58.0 (-7.2%)

These simple models with comparable module sizes across methods isolate the impact of C3T's novel technique, demonstrating its efficacy independent of complex architectures or larger datasets. This approach facilitates potential future scaling and expansion of the method.

Datasets and Hyperparameters: We present results on four diverse datasets: (1) UTD-MHAD [19], a small yet structured dataset; (2) CZU-MHAD [20], a slightly larger dataset captured in a controlled environment; (3) MMACT [16], a very large dataset with various challenges including different view-angles, scenes, and occlusions; and (4) MMEA-CL [21], an egocentric camera dataset. For each dataset, we create an approximately 40-40-10-10 percent data split for the $\mathcal{D}_{\text{Align}}$, \mathcal{D}_{HAR} , \mathcal{D}_{Val} , and $\mathcal{D}_{\text{Test}}$ sets respectively, as shown in Appendix Table 9. \mathcal{D}_{Val} was used to perform a minor hyperparameter search on the UTD-MHAD dataset. The methods performed best with a learning rate of 1.5×10^{-4} , a batch size of 16, and a latent representation dimension of 2048 with an Adam optimizer. The preprocessing steps downsample the video to $t = 30$ frames, and C3T extracts $t_{\text{fm}} = 15$ latent vectors per sample. Experiments were implemented in Pytorch and run on a 16GB NVIDIA Quadro RTX 5000, four 48GB A40s, or four 48GB A100s. More detailed information about each dataset and implementation can be found in Appendix Section 7.7.

UMA vs Supervised Settings: Our results in Table 1 show Top-1 and Top-3 test accuracies on 4 different datasets. Along with the UMA setting, we show the results of our architecture under complete supervision: the IMU row trains $f^{(1)} : \mathcal{X}^{(IMU)} \rightarrow \mathcal{Y}$, RGB trains $f^{(2)} : \mathcal{X}^{(RGB)} \rightarrow \mathcal{Y}$, and $Fusion$ averages the outputs of $f^{(1)}$ and $f^{(2)}$ and trains a linear head h . The *Random* row shows the probability of guessing the correct class, assuming a uniform distribution. We run each experiment thrice with different random seeds, reporting the average accuracies to ensure rigorous empirical results. Appendix Figure 11 shows all the runs, the computed averages, and their corresponding standard deviations.

The experimental results in the UMA setting consistently rank C3T as the most accurate, followed by CA, and then ST. Despite its lower ranking, ST shows a 3-10x improvement over random prediction, indicating some efficacy in UMA. We attribute ST's limited performance to its reliance on the teacher model's accuracy and its inability to leverage multimodal correlations in a latent space. Figure 5 supports this conclusion by illustrating how contrastive alignment encourages multimodal representations to cluster by class prior to label introduction. We hypothesize that C3T outperforms CA by aligning modalities across a larger temporal representation space, enabling it to capture more detailed temporal information.

Finally, another notable result from Table 1 is that on UTD-MHAD Top-1 and MMEA-CL Top-3 accuracies, C3T surpasses the supervised RGB model. This may imply that cross-modal temporal alignment may uncover an inherent correlation between the modalities more informative than the label information.

Accuracy vs Latent Size: Figure 3 illustrates the UMA performance across different latent vector sizes. Since ST does not utilize a latent vector, we adjust the hidden size of its final MLP, observing relatively consistent performance. Furthermore, CA’s performance declines significantly with smaller latent vectors, whereas C3T maintains superior performance even at reduced model sizes. Notably, C3T’s size scales efficiently as the self-attention head size decreases significantly with reduced input token dimensions, underscoring C3T’s suitability for resource-constrained environments such as on-device computing for wearables or smart devices.

UMA in Temporal Noise: We evaluated each method’s robustness to temporal noise during testing, simulating three real-life scenarios (Table 2):

1. **Crop:** Randomly shifts and crops both modalities’ time sequences by up to 60%, simulating continuous real-time action recognition, where an action may not occur in the middle of the time sequence.
2. **Misalign:** Applies crop to one modality, mimicking hardware asynchrony or differing frame rates.
3. **Dilation:** Applies crop to both modalities and then upsamples, imitating slower action movements.
4. **All:** Applies all the types of noise to each data sample.

C3T demonstrates robust performance under temporal noise, likely due to its attention-based HAR module leveraging tokens generated by the feature map of a temporal convolution. The self-attention mechanism compares neighboring tokens from various time sections, effectively capturing actions regardless of their temporal position within the sequence. Figure 4 visualizes the attention weights of the latent vectors in C3T’s self-attention head when the input sample is cropped and shifted. Interestingly, **the shifted input results in a corresponding shift in the attention scores, illustrating its robustness toward this noise pattern.** Additionally, due to the design of the self-attention block, C3T’s HAR head is invariant to variable-length inputs during inference, which provides an advantage in cropped scenarios, requiring minimal zero-padding compared to the ST and CA methods.

Ablations: To demonstrate that C3T’s performance advantage stems from its temporal alignment approach rather than its self-attention HAR module, we conducted comprehensive ablation studies on UTD-MHAD. Our results show two key findings: (1) adding attention mechanisms to ST or CA frameworks fails to match C3T’s performance, and (2) C3T maintains superior performance over both methods even without its attention module.

First, we compare UMA performance using convolution and attention-based feature extractors. The RGB encoder has two feature extraction steps (spatial and temporal) and IMU has one (temporal). Table 3 indicates that ST or CA with attention do not perform as well even with larger parameter sizes. This aligns with previous work showing that convolutions are superior to attention for IMU data [26], and visual attentions works less well on small-scale datasets [22].

We further ablate C3T head architectures (Table 4). We test two attention-based heads and two MLP heads that condense the $Z_1 \dots Z_{t_{\text{rec}}}$ latent vectors into a single output class. The first attention head uses a class token as shown in Figure 2, and the second concatenates all the output tokens and projects it to an output. The MLP methods either add or concatenate all the temporal features before passing it through an MLP. While concatenating latent vectors and using an MLP performed best on clean data (78.8%), the class token mechanism offered superior robustness to noise and was thus chosen for C3T. **Furthermore, all C3T variants in Table 4 outperform CA and ST in UMA performance (12.9% and 42.6% respectively from Table 1), emphasizing C3T’s**

Table 3: **Architecture Ablation:** Encoder types are reported as (RGB-Spatial / RGB-Temporal / IMU-Temporal), where C = Convolution and A = Attention.

Method	Encoders	Params (M)	Acc. (%)
ST [14]	C/C/C	129.2	12.9
	C/C/A	97.8	10.2
	C/A/C	871.2	11.4
	A/C/C	291.5	5.7
CA [3]	C/C/C	163.8	42.6
	C/C/A	132.3	19.3
	C/A/C	905.7	34.1
	A/C/C	326.0	26.1
C3T	C/C/C	137.7	62.5
	C/C/A	106.3	15.9
	C/A/C	879.6	53.4
	A/C/C	300.0	33.0

Table 4: **C3T HAR Module Ablations:** Comparison of 2 Attention methods and two MLP methods.

Input	Attention		MLP	
	Cls Token	Concat.	Add	Concat.
Clean	62.5	44.32	56.82	70.45
Noisy	52.27	43.18	50.00	43.18

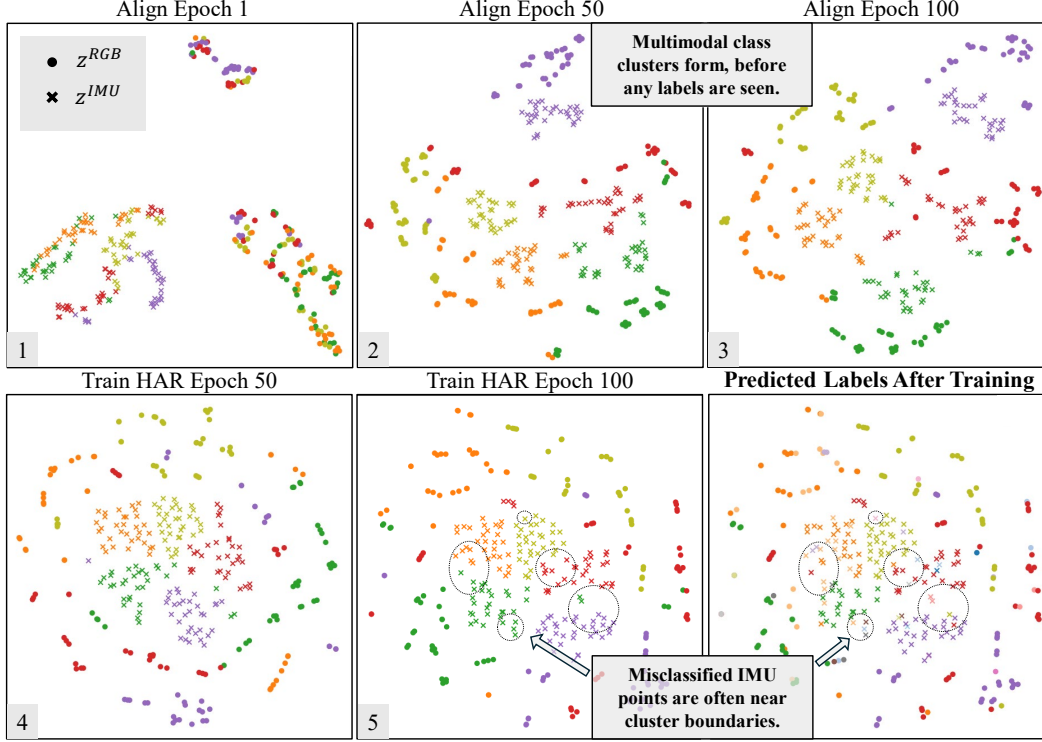


Figure 5: **CA TSNE Plots in UMA:** The following shows the progression of the latent representations of datapoints for 5 classes (Bowling, Clap, Draw circle (clockwise), Jog, Basketball shoot) during training CA on the UTD-MHAD dataset. In the end, we plot the predicted labels and circle areas of confusion, which seem to often occur at the boundaries between clusters.

strength lies in temporal alignment, not its attention mechanism. The key distinction between CA and C3T+Concat-MLP is where the feature vectors are combined: CA condenses the convolution output map to one feature vector before alignment, while C3T does so post-alignment for the HAR task. This suggests that effective cross-modal knowledge transfer at the local feature level is crucial for time-series data, with global features being more appropriately utilized for post-transfer inference.

5 Additional Experiments and Discussion

How do we train the CA and C3T Architectures?

- (1) **Align First:** First aligns the representations generated by the RGB and IMU encoders, $f^{(1)}$ and $f^{(2)}$ RGB on $\mathcal{D}_{\text{Align}}$ (phase b depicted in Figure 2). Then it freezes the weights for both encoders and trains the HAR module h on RGB data in \mathcal{D}_{HAR} (phase a in Figure 2).
- (2) **HAR First:** Reverses the order from 1. First it performs phase a , RGB HAR training, then it freezes the RGB encoder $f^{(1)}$ and aligns the IMU encoder $f^{(2)}$, phase b .
- (3) **Interspersed Training:** Intermittently learns from $\mathcal{D}_{\text{Align}}$ and \mathcal{D}_{HAR} . The model learns an epoch from phase a and updates its weights to train the RGB HAR model, then learns an epoch from phase b and updates its weights to align the encoders, iterating between the two losses.
- (4) **Combined Loss:** Train both phase a and phase b but within the same loss iteration. The loss from phase a on a batch of data from \mathcal{D}_{HAR} is added to the loss from phase b on a batch of data from $\mathcal{D}_{\text{Align}}$ and the total is used to update the weights: $\mathcal{L}_{\text{Total}} = \mathcal{L}_{\text{CE}} + \mathcal{L}_{\text{CL/C3T}}$.

Results: As shown in the Table 5, training by the *Align First* method performs the best for C3T, whereas *Combined Loss* performs the best for CA. The main experiments reported in this work (Table 1) use training methods *Align First* and *Combined Loss* for C3T and CA, respectively. We hypothesize that *HAR First* yields a latent space tailored to RGB HAR, which does not capture IMU-RGB correlations, and *Interspersed Training* faces instability in training.

Table 5: **Additional Experiments:** Performance of ST, CA, and C3T across various training methods, testing modalities, and reverse transfer from IMU to RGB data (RT). See Section 5 for details.

Model	Training Method				Modality Testing			RT
	(1)	(2)	(3)	(4)	(1) IMU	(2) RGB	(3) Both	I→R
ST [14]	-	-	-	-	12.9	53.8	17.0	4.60
CA [3]	38.6	36.4	27.3	42.6	42.6	56.8	60.2	27.3
C3T	62.5	35.2	51.1	27.9	62.5	78.4	79.5	31.8

Figure 5 visualizes the latent space outputs of CA training with the *Align First* method using t-SNE plots [28]. The model quickly segments classes during the align phase, even without labels, suggesting that the data’s natural structure facilitates class distinction across different modalities. This supports the Platonic Representation Hypothesis [29] which posits that the same semantic concepts learned from different modalities or data-views are converging to some ground-truth concept space. The separable clusters also imply that CA and C3T could potentially adapt to new class labels with just a few samples, as the latent structure would have already grouped similar classes. Furthermore, after training, the model tends to misclassify points near the boundary between clusters, implying that the HAR head is learning a decision boundary in this latent space. **Figure 5 supports our initial hypothesis (Figure 1) that a joint latent space could be leveraged to perform UMA using a classification head trained only on RGB data.**

Can UMA methods retain performance on the labeled modality or leverage both modalities?

- (1) **IMU (UMA):** Is the main result of this paper and described above in Section 3.
- (2) **RGB (Supervised Learning):** Tests the model on RGB data, which was labeled during training.
- (3) **Both (Sensor Fusion):** Merges latent vectors from each modality by adding them.

Results: Table 5 shows that C3T outperforms the other methods. When comparing the performances in the different test scenarios, our experiments indicate that when given both modalities, fusion performs better than the RGB model alone. Instead of introducing noise or uncertainty into the model, introducing an unlabeled modality may add structure to the shared latent space that bolsters performance, especially if that modality is highly informative for the given task. This observation bears resemblance to knowledge distillation methods, where an auxiliary modality during training leads to improved testing outcomes; however, these methods usually assume that auxiliary modality is labeled [30]. Applying UMA to sensor fusion presents a promising avenue for future research.

Can the transfer be performed in reverse?

To transfer from IMU to RGB data C3T trains on labeled IMU data and unlabeled IMU+RGB data, then tests on unlabeled RGB data. The results in the I→R column of Table 5 indicate that C3T’s superior performance generalizes to this new configuration. Furthermore, the performance is worse when transferring from IMU to RGB, implying that transfer from a more informative data modality (RGB) to a less informative one (IMU) is more effective. This aligns with our initial motivation that RGB data is more abundant and easier to label, and RGB to IMU has more real-world applications, such as transferring from a smart home camera to a smartwatch as outlined in Figure 1. Nonetheless, further analysis C3T in various scenarios and modalities is a relevant future research extension.

The supplementary Appendix contains current status of existing related literature 7.1, a deeper discussion of future directions and limitations (Section 7.3) as well as additional visualizations (Section 7.2), experiments (Section 7.4), ablations (Section 7.5), implementation details (Sections 7.6 and 7.7) and baselines (Section 7.8).

6 Conclusion

We explored the UMA framework for human action recognition, challenging models to perform inference on a modality that was unlabeled during training. Our experiments focused on constructing a unified latent space between modalities and comparing three UMA methods in various settings. Our C3T method, which performs alignment on local temporal latent tokens, showed promising results for robust cross-modal transfer in UMA. We hope that our results inspire further exploitation of cross-modal latent spaces for more robust human motion understanding with AI models.

Acknowledgments and Disclosure of Funding

This material is based upon work supported by the National Science Foundation (NSF) Graduate Research Fellowship Program. We acknowledge the NSF for providing access to the NCSA Delta GPU cluster (A100 and A40 GPUs) under the NSF ACCESS program (allocation project CIS240405). This resource enabled the computational experiments critical to this research.

References

- [1] Seungwhan Moon, Andrea Madotto, Zhaojiang Lin, Alireza Dirafzoon, Aparajita Saraf, Amy Bearman, and Babak Damavandi. Imu2clip: Multimodal contrastive learning for imu motion sensors from egocentric videos and text. *arXiv preprint arXiv:2210.14395*, 2022.
- [2] Rohit Girdhar, Alaaeldin El-Nouby, Zhuang Liu, Mannat Singh, Kalyan Vasudev Alwala, Armand Joulin, and Ishan Misra. Imagebind: One embedding space to bind them all. In *Proceedings of the IEEE/CVF Conference on Computer Vision and Pattern Recognition*, pages 15180–15190, 2023.
- [3] Xinyu Gong, Sreyas Mohan, Naina Dhirga, Jean-Charles Bazin, Yilei Li, Zhangyang Wang, and Rakesh Ranjan. Mmg-ego4d: Multimodal generalization in egocentric action recognition. In *Proceedings of the IEEE/CVF Conference on Computer Vision and Pattern Recognition*, pages 6481–6491, 2023.
- [4] Vimal Mollyn, Riku Arakawa, Mayank Goel, Chris Harrison, and Karan Ahuja. Imuposer: Full-body pose estimation using imus in phones, watches, and earbuds. In *Proceedings of the 2023 CHI Conference on Human Factors in Computing Systems*, pages 1–12, 2023.
- [5] Shuteng Niu, Yongxin Liu, Jian Wang, and Houbing Song. A decade survey of transfer learning (2010–2020). *IEEE Transactions on Artificial Intelligence*, 1(2):151–166, 2020.
- [6] Sungtae An, Alessio Medda, Michael N Sawka, Clayton J Hutto, Mindy L Millard-Stafford, Scott Appling, Kristine LS Richardson, and Omer T Inan. Adaptnet: human activity recognition via bilateral domain adaptation using semi-supervised deep translation networks. *IEEE Sensors Journal*, 21(18):20398–20411, 2021.
- [7] Sangmin Woo, Sumin Lee, Yeonju Park, Muhammad Adi Nugroho, and Changick Kim. Towards good practices for missing modality robust action recognition. In *Proceedings of the AAAI Conference on Artificial Intelligence*, volume 37, pages 2776–2784, 2023.
- [8] Nuno C Garcia, Pietro Morerio, and Vittorio Murino. Modality distillation with multiple stream networks for action recognition. In *Proceedings of the European Conference on Computer Vision (ECCV)*, pages 103–118, 2018.
- [9] Qi Wang, Liang Zhan, Paul Thompson, and Jiayu Zhou. Multimodal learning with incomplete modalities by knowledge distillation. In *Proceedings of the 26th ACM SIGKDD International Conference on Knowledge Discovery & Data Mining*, pages 1828–1838, 2020.
- [10] Muhammad Adi Nugroho, Sangmin Woo, Sumin Lee, and Changick Kim. Ahfu-net: Align, hallucinate, and fuse network for missing multimodal action recognition. In *2023 IEEE International Conference on Visual Communications and Image Processing (VCIP)*, pages 1–5. IEEE, 2023.
- [11] Lijin Yang, Yifei Huang, Yusuke Sugano, and Yoichi Sato. Interact before align: Leveraging cross-modal knowledge for domain adaptive action recognition. In *Proceedings of the IEEE/CVF conference on computer vision and pattern recognition*, pages 14722–14732, 2022.
- [12] Youngjae Chang, Akhil Mathur, Anton Isopoussu, June-hwa Song, and Fahim Kawsar. A systematic study of unsupervised domain adaptation for robust human-activity recognition. *Proceedings of the ACM on Interactive, Mobile, Wearable and Ubiquitous Technologies*, 4(1): 1–30, 2020.
- [13] Abhi Kamboj and Minh Do. A survey of imu based cross-modal transfer learning in human activity recognition. *arXiv preprint arXiv:2403.15444*, 2024.

- [14] Fida Mohammad Thoker and Juergen Gall. Cross-modal knowledge distillation for action recognition. In *2019 IEEE International Conference on Image Processing (ICIP)*, pages 6–10. IEEE, 2019.
- [15] Zihui Xue, Zhengqi Gao, Sucheng Ren, and Hang Zhao. The modality focusing hypothesis: Towards understanding crossmodal knowledge distillation. *arXiv preprint arXiv:2206.06487*, 2022.
- [16] Quan Kong, Ziming Wu, Ziwei Deng, Martin Klinkigt, Bin Tong, and Tomokazu Murakami. Mmact: A large-scale dataset for cross modal human action understanding. In *Proceedings of the IEEE/CVF International Conference on Computer Vision*, pages 8658–8667, 2019.
- [17] XB Bruce, Yan Liu, and Keith CC Chan. Multimodal fusion via teacher-student network for indoor action recognition. In *Proceedings of the AAAI Conference on Artificial Intelligence*, volume 35(4), pages 3199–3207, 2021.
- [18] Alec Radford, Jong Wook Kim, Chris Hallacy, Aditya Ramesh, Gabriel Goh, Sandhini Agarwal, Girish Sastry, Amanda Askell, Pamela Mishkin, Jack Clark, et al. Learning transferable visual models from natural language supervision. In *International Conference on Machine Learning*, pages 8748–8763. PMLR, 2021.
- [19] Chen Chen, Roozbeh Jafari, and Nasser Kehtarnavaz. Utd-mhad: A multimodal dataset for human action recognition utilizing a depth camera and a wearable inertial sensor. In *2015 IEEE International conference on image processing (ICIP)*, pages 168–172. IEEE, 2015.
- [20] Xin Chao, Zhenjie Hou, and Yujian Mo. Czu-mhad: A multimodal dataset for human action recognition utilizing a depth camera and 10 wearable inertial sensors. *IEEE Sensors Journal*, 22(7):7034–7042, 2022.
- [21] Linfeng Xu, Qingbo Wu, Lili Pan, Fanman Meng, Hongliang Li, Chiyuan He, Hanxin Wang, Shaoxu Cheng, and Yu Dai. Towards continual egocentric activity recognition: A multi-modal egocentric activity dataset for continual learning. *IEEE Transactions on Multimedia*, 2023.
- [22] Alexey Dosovitskiy, Lucas Beyer, Alexander Kolesnikov, Dirk Weissenborn, Xiaohua Zhai, Thomas Unterthiner, Mostafa Dehghani, Matthias Minderer, Georg Heigold, Sylvain Gelly, et al. An image is worth 16x16 words: Transformers for image recognition at scale. *arXiv preprint arXiv:2010.11929*, 2020.
- [23] Kensho Hara, Hirokatsu Kataoka, and Yutaka Satoh. Learning spatio-temporal features with 3d residual networks for action recognition. In *Proceedings of the IEEE international conference on computer vision workshops*, pages 3154–3160, 2017.
- [24] Du Tran, Heng Wang, Lorenzo Torresani, Jamie Ray, Yann LeCun, and Manohar Paluri. A closer look at spatiotemporal convolutions for action recognition. In *Proceedings of the IEEE conference on Computer Vision and Pattern Recognition*, pages 6450–6459, 2018.
- [25] Joao Carreira and Andrew Zisserman. Quo vadis, action recognition? a new model and the kinetics dataset. In *proceedings of the IEEE Conference on Computer Vision and Pattern Recognition*, pages 6299–6308, 2017.
- [26] E Valarezo, P Rivera, JM Park, G Gi, TY Kim, MA Al-Antari, M Al-Masni, and T-S Kim. Human activity recognition using a single wrist imu sensor via deep learning convolutional and recurrent neural nets. *Journal of ICT, Design, Engineering and Technological Science*, pages 1–5, 2017.
- [27] Oumaima Moutik, Hiba Sekkat, Smail Tigani, Abdellah Chehri, Rachid Saadane, Taha Ait Tchakoucht, and Anand Paul. Convolutional neural networks or vision transformers: Who will win the race for action recognitions in visual data? *Sensors*, 23(2):734, 2023.
- [28] Laurens Van der Maaten and Geoffrey Hinton. Visualizing data using t-sne. *Journal of machine learning research*, 9(11), 2008.
- [29] Minyoung Huh, Brian Cheung, Tongzhou Wang, and Phillip Isola. Position: The platonic representation hypothesis. In *Forty-first International Conference on Machine Learning*, 2024.

- [30] Mengxi Chen, Linyu Xing, Yu Wang, and Ya Zhang. Enhanced multimodal representation learning with cross-modal kd. In *Proceedings of the IEEE/CVF Conference on Computer Vision and Pattern Recognition*, pages 11766–11775, 2023.
- [31] Sinno Jialin Pan and Qiang Yang. A survey on transfer learning. *IEEE Transactions on knowledge and data engineering*, 22(10):1345–1359, 2009.
- [32] Abolfazl Farahani, Sahar Voghoei, Khaled Rasheed, and Hamid R Arabnia. A brief review of domain adaptation. *Advances in data science and information engineering: proceedings from ICDATA 2020 and IKE 2020*, pages 877–894, 2021.
- [33] Sejal Bhalla, Mayank Goel, and Rushil Khurana. Imu2doppler: Cross-modal domain adaptation for doppler-based activity recognition using imu data. *Proceedings of the ACM on Interactive, Mobile, Wearable and Ubiquitous Technologies*, 5(4):1–20, 2021.
- [34] Jindong Wang, Vincent W Zheng, Yiqiang Chen, and Meiyu Huang. Deep transfer learning for cross-domain activity recognition. In *proceedings of the 3rd International Conference on Crowd Science and Engineering*, pages 1–8, 2018.
- [35] Aria Ghora Prabono, Bernardo Nugroho Yahya, and Seok-Lyong Lee. Hybrid domain adaptation with deep network architecture for end-to-end cross-domain human activity recognition. *Computers & Industrial Engineering*, 151:106953, 2021.
- [36] Rong Hu, Ling Chen, Shenghuan Miao, and Xing Tang. Swl-adapt: An unsupervised domain adaptation model with sample weight learning for cross-user wearable human activity recognition. In *Proceedings of the AAAI Conference on artificial intelligence*, volume 37(5), pages 6012–6020, 2023.
- [37] Zhongzheng Fu, Xinrun He, Enkai Wang, Jun Huo, Jian Huang, and Dongrui Wu. Personalized human activity recognition based on integrated wearable sensor and transfer learning. *Sensors*, 21(3):885, 2021.
- [38] Md Abdullah Al Hafiz Khan, Nirmalya Roy, and Archan Misra. Scaling human activity recognition via deep learning-based domain adaptation. In *2018 IEEE international conference on pervasive computing and communications (PerCom)*, pages 1–9. IEEE, 2018.
- [39] Zhijun Zhou, Yingtian Zhang, Xiaojing Yu, Panlong Yang, Xiang-Yang Li, Jing Zhao, and Hao Zhou. Xhar: Deep domain adaptation for human activity recognition with smart devices. In *2020 17th Annual IEEE International Conference on Sensing, Communication, and Networking (SECON)*, pages 1–9. IEEE, 2020.
- [40] Avijoy Chakma, Abu Zaher Md Faridee, Md Abdullah Al Hafiz Khan, and Nirmalya Roy. Activity recognition in wearables using adversarial multi-source domain adaptation. *Smart Health*, 19:100174, 2021.
- [41] Hyeokhyen Kwon, Catherine Tong, Harish Haresamudram, Yan Gao, Gregory D Abowd, Nicholas D Lane, and Thomas Ploetz. Imutube: Automatic extraction of virtual on-body accelerometry from video for human activity recognition. *Proceedings of the ACM on Interactive, Mobile, Wearable and Ubiquitous Technologies*, 4(3):1–29, 2020.
- [42] Yujiao Hao, Xijian Lou, Boyu Wang, and Rong Zheng. Cromosim: A deep learning-based cross-modality inertial measurement simulator. *IEEE Transactions on Mobile Computing*, 2022.
- [43] Zhan Tong, Yibing Song, Jue Wang, and Limin Wang. Videomae: Masked autoencoders are data-efficient learners for self-supervised video pre-training. *Advances in neural information processing systems*, 35:10078–10093, 2022.
- [44] Md Mofijul Islam, Mohammad Samin Yasar, and Tariq Iqbal. Maven: A memory augmented recurrent approach for multimodal fusion. *IEEE Transactions on Multimedia*, 2022.
- [45] Liang Shi, Yixin Chen, Meimei Liu, and Feng Guo. Dust: Dual swin transformer for multimodal video and time-series modeling. In *Proceedings of the IEEE/CVF Conference on Computer Vision and Pattern Recognition*, pages 4537–4546, 2024.

- [46] Jiaojiao Zhao, Yanyi Zhang, Xinyu Li, Hao Chen, Bing Shuai, Mingze Xu, Chunhui Liu, Kaustav Kundu, Yuanjun Xiong, Davide Modolo, et al. Tuber: Tubelet transformer for video action detection. In *Proceedings of the IEEE/CVF Conference on Computer Vision and Pattern Recognition*, pages 13598–13607, 2022.
- [47] Yimu Wang, Kun Yu, Yan Wang, and Hui Xue. Multi-view fusion transformer for sensor-based human activity recognition. *arXiv preprint arXiv:2202.12949*, 2022.
- [48] Anurag Arnab, Mostafa Dehghani, Georg Heigold, Chen Sun, Mario Lučić, and Cordelia Schmid. Vivit: A video vision transformer. In *Proceedings of the IEEE/CVF international conference on computer vision*, pages 6836–6846, 2021.
- [49] Ze Liu, Jia Ning, Yue Cao, Yixuan Wei, Zheng Zhang, Stephen Lin, and Han Hu. Video swin transformer. In *Proceedings of the IEEE/CVF conference on computer vision and pattern recognition*, pages 3202–3211, 2022.
- [50] Dhanesh Ramachandram and Graham W Taylor. Deep multimodal learning: A survey on recent advances and trends. *IEEE signal processing magazine*, 34(6):96–108, 2017.
- [51] Sharmin Majumder and Nasser Kehtarnavaz. Vision and inertial sensing fusion for human action recognition: A review. *IEEE Sensors Journal*, 21(3):2454–2467, 2020.
- [52] Rajeev Sharma, Vladimir I Pavlovic, and Thomas S Huang. Toward multimodal human-computer interface. *Proceedings of the IEEE*, 86(5):853–869, 1998.
- [53] Md Mofijul Islam and Tariq Iqbal. Hamlet: A hierarchical multimodal attention-based human activity recognition algorithm. In *2020 IEEE/RSJ International Conference on Intelligent Robots and Systems (IROS)*, pages 10285–10292. IEEE, 2020.
- [54] Haoran Wei, Roozbeh Jafari, and Nasser Kehtarnavaz. Fusion of video and inertial sensing for deep learning-based human action recognition. *Sensors*, 19(17):3680, 2019.

7 Appendix: Related Works, Additional Description and Visualizations

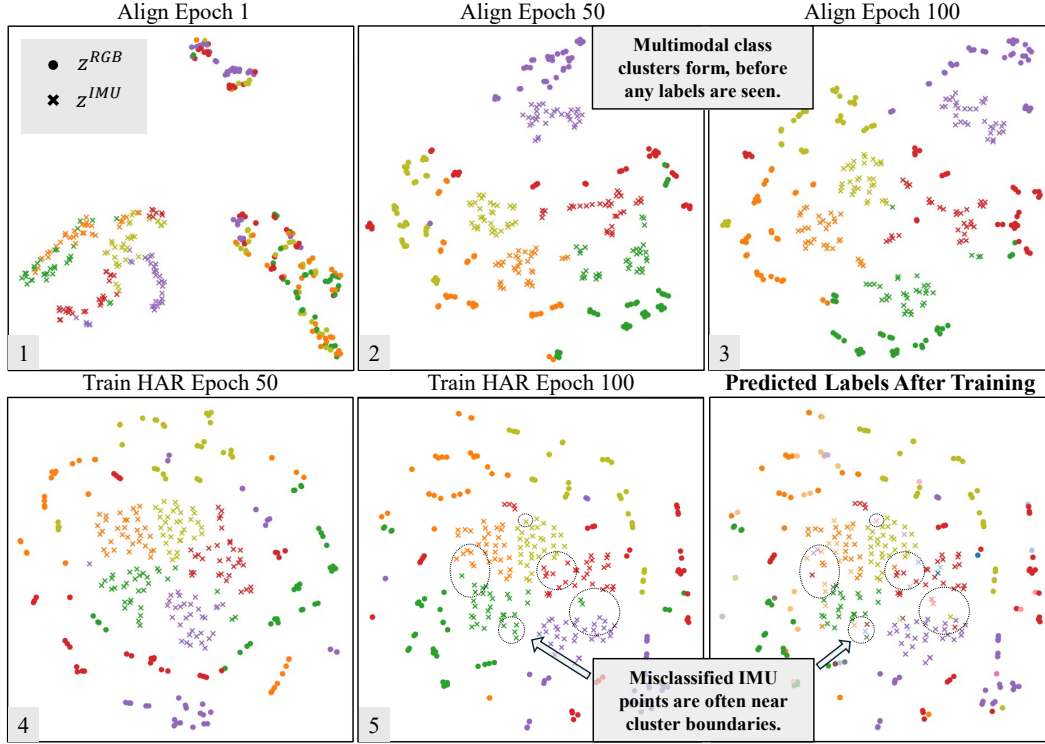


Figure 6: **CA TSNE Plots in UMA:** (Reproduced Figure 5 Larger) The following shows the progression of the latent representations of datapoints for 5 classes (Bowling, Clap, Draw circle (clockwise), Jog, Basketball shoot) during training CA on the UTD-MHAD dataset. In the end, we plot the predicted labels and circle areas of confusion, which seem to often occur at the boundaries between clusters.

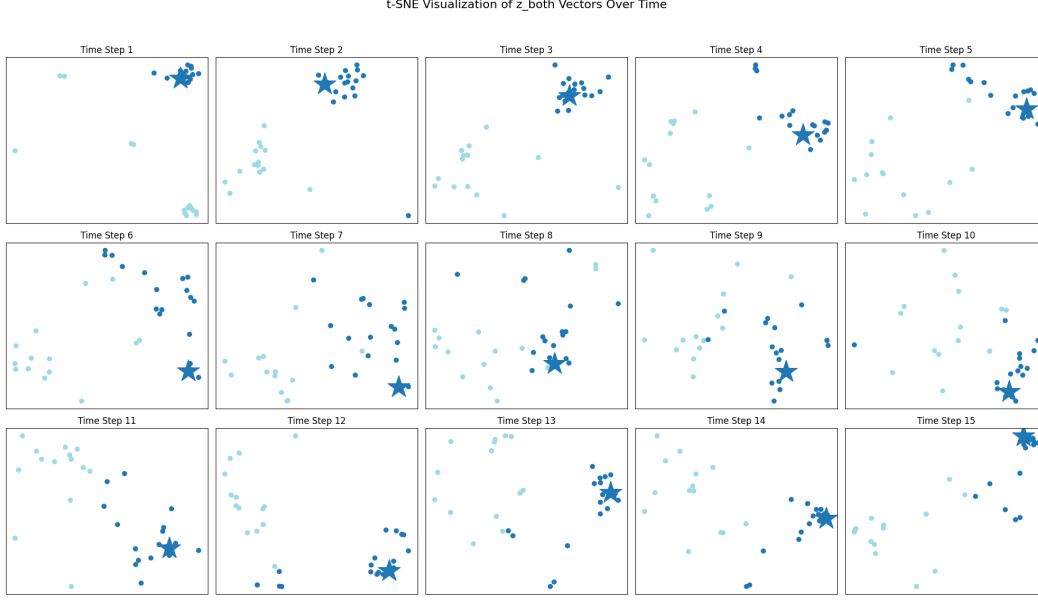


Figure 7: **C3T TSNE plot with shifted input:** This plot visualizes the TSNE plots of the $t_{rec} = 15$ latent $z_i = 0 \dots t_{rec}$ for various points of two classes. The z s shown are the fused representation between the IMU and RGB modalities. The dark blue star is a point that was *shifted by 50%* compared to the rest of the visualized points for the class. Notice how some time steps are more distinctive than others between the classes, and the star tends towards the edge of the group for many z s.

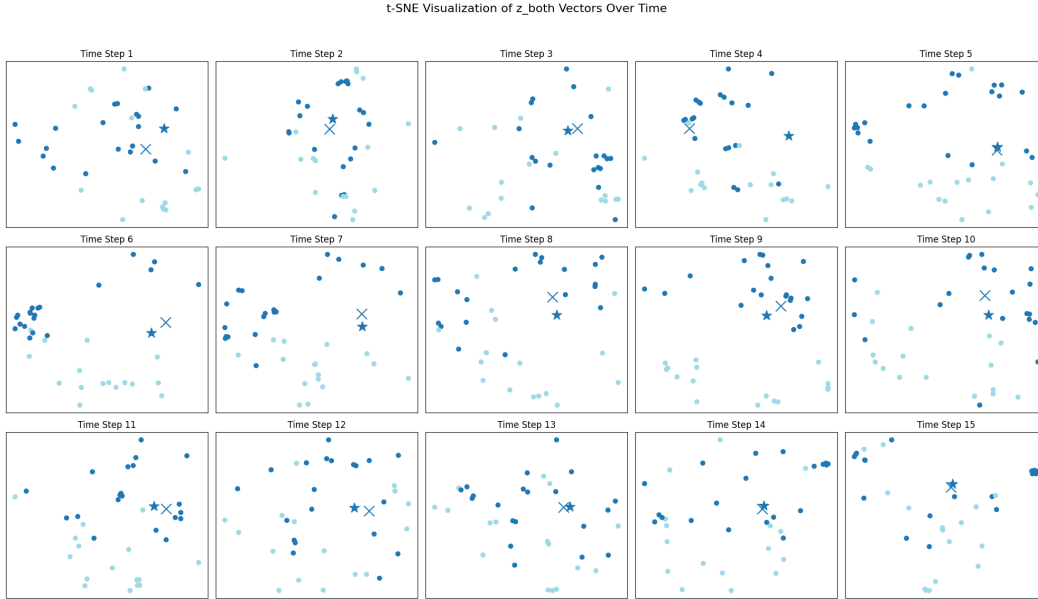


Figure 8: **C3T TSNE plot with shifted input:** Another TSNE plot with shifted input for different classes from the previous figure (Dark blue shows 'Swipe left' and light blue shows 'Pick up and throw'). This time X marks the regular input and star marks the shifted inputs. Unexpectedly, they are relatively close through out, indicating the temporal convolutions that constructed these z 's might be doing part of the work when accounting for robustness to shift noise. Furthermore, notice how z_7 to z_{10} indicate latent variables that are more distinctive (there is a more clear boundary between the light blue and dark blue points). This could indicate that these time steps are most important for distinguishing between the two given classes.

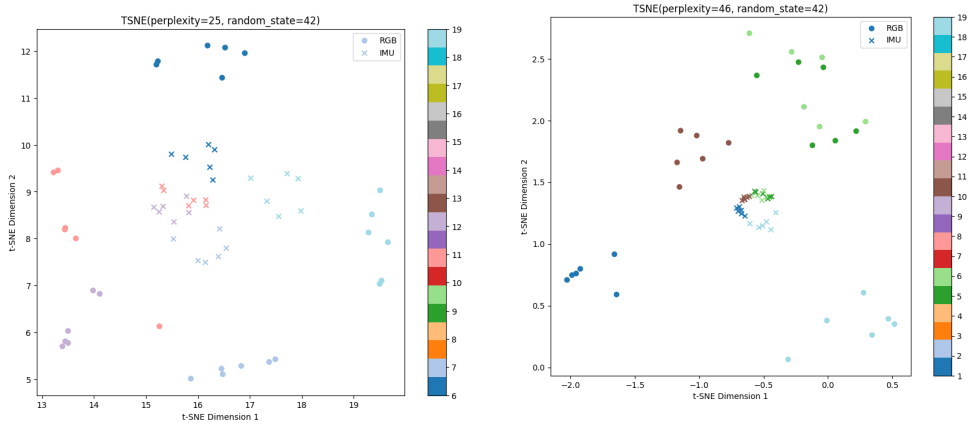


Figure 9: **CA TSNE on CZU Dataset:** These plots indicate the same trend discussed in the main paper, that the IMU points in the multimodal representation space tend to cluster in the middle and mirror the RGB points on the outside. Particularly, for the CZU dataset the IMU signals are stronger (60 IMU channels, 6 on 10 wearable devices) and this clustering tends to be stronger.

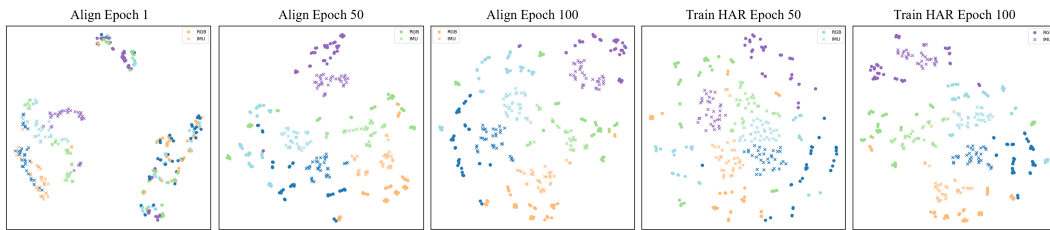


Figure 10: **CA TSNE Plots:** These are similar to the plot shown in the main paper Figure 5, but with different classes. The following shows the progression of the latent representations for 5 classes (5 different colors) during training CA on the UTD-MHAD dataset in UMA. Circles indicate RGB data, and crosses indicate IMU data points.

		UTD							MMACT							MMEA							CZU						
		Top 1	Top3	Top5	Top7	Top7	Top7	Top7	Top 1	Top3	Top5	Top7	Top7	Top7	Top7	Top 1	Top3	Top5	Top7	Top7	Top7	Top7	Top 1	Top3	Top5	Top7	Top7	Top7	Top7
Supervised	RGB	trial1	61.36364	75	79.54546	82.95454	42.37689	63.26291	74.53052	82.39436	56.70732	79.87805	86.28049	91.46342	94.44286	100	100	100	100	100	100	94.44286	100	100	100	100	100	100	100
		trial2	61.36364	79.54546	86.36364	90.90909	41.19718	59.50704	69.71831	79.10798	56.09766	78.5061	85.97961	89.93903	96.42857	100	100	100	100	100	100	96.42857	100	100	100	100	100	100	100
		trial3	38.63636	64.77273	67.04546	72.72727	42.69563	62.9892	72.1831	79.05164	49.84766	72.85585	80.18334	89.97561	91.07143	96.10714	99.10714	100	100	100	100	91.07143	96.10714	99.10714	99.10714	100	100	100	100
		avg	53.79368	73.16636	77.65152	82.19697	42.05709	61.61072	72.14398	79.85133	54.97348	72.08333	84.14834	89.17602	94.07362	96.70238	99.70238	100	100	100	100	94.07362	96.70238	99.70238	99.70238	100	100	100	100
		std	13.1216	7.56283	9.797361	8.11453	0.754589	1.321445	2.406344	2.26478	3.798723	3.716307	3.4358	2.6328	2.727723	0.515483	0.515483	0.515483	0	0	0	2.727723	0.515483	0.515483	0.515483	0	0	0	0
Supervised	IMU	trial1	87.5	97.72727	97.72727	97.72727	69.24883	90.14085	95.30516	96.50999	65.70122	87.5	92.68593	96.18903	94.64286	96.21429	98.21429	100	100	100	100	94.64286	96.21429	98.21429	98.21429	100	100	100	100
		trial2	87.5	97.72727	97.72727	97.72727	70.30516	90.14085	94.95305	96.71362	66.46342	87.80488	93.14024	95.27439	95.53571	96.21429	98.21429	100	100	100	100	95.53571	96.21429	98.21429	98.21429	100	100	100	100
		trial3	88.63636	97.72727	97.72727	97.72727	70.30516	89.78873	94.95305	96.71362	65.2439	87.5	92.53049	95.42683	94.64286	96.21429	98.21429	100	100	100	100	94.64286	96.21429	98.21429	98.21429	100	100	100	100
		avg	87.87079	97.72727	97.72727	97.72727	69.95305	90.02348	95.07042	96.67449	65.02585	87.60163	92.78455	95.63008	94.94048	96.21429	98.80953	100	100	100	100	94.94048	96.21429	98.80953	98.80953	100	100	100	100
		std	0.656078	1.74E-14	1.74E-14	1.74E-14	0.609872	0.203297	0.203297	0.179291	0.616079	0.176023	0.317324	0.490076	0.515487	0	0.103098	0	0	0	0	0.515487	0	0.103098	0	0	0	0	0
Supervised	FUSION	trial1	64.77273	87.5	92.04546	94.31818	77.34742	92.13815	94.71831	96.12676	83.84146	94.96951	96.95122	97.40854	95.53571	98.21429	99.10714	100	100	100	100	95.53571	98.21429	99.10714	99.10714	100	100	100	100
		trial2	51.13636	76.13636	81.81818	86.36364	75.93896	90.96244	95.89202	97.65258	71.18903	86.26219	92.22961	94.05488	93.75	99.10714	100	100	100	100	100	93.75	99.10714	100	100	100	100	100	100
		trial3	71.50991	82.95454	86.63636	89.77273	76.87794	92.95775	95.53991	96.3615	85.21342	94.81707	96.79978	97.40854	95.53571	98.21429	99.10714	100	100	100	100	95.53571	98.21429	99.10714	99.10714	100	100	100	100
		avg	62.5	82.19697	87.5	90.15152	76.72144	92.01878	95.38341	96.71361	80.0813	92.68292	95.3252	96.29065	94.94047	96.51191	99.40476	99.70238	100	100	100	94.94047	96.51191	99.40476	99.70238	100	100	100	100
		std	10.41485	5.719573	5.207475	3.980775	0.717153	1.00282	0.602302	0.821596	7.731427	3.832226	2.685408	1.936237	1.03098	0.515487	0.515483	0.515483	0.515483	0.515483	0.515483	1.03098	0.515487	0.515483	0.515483	0.515483	0.515483	0.515483	0.515483
UMA	ST	trial1	15.90909	27.27273	32.95454	37.5	17.60583	37.0892	48.34366	56.69014	9.60388	23.17073	30.79586	38.71951	40.17857	59.82743	70.53571	79.46429	86.36364	91.07143	96.21429	40.17857	59.82743	70.53571	79.46429	86.36364	91.07143	96.21429	100
		trial2	13.63636	22.72727	30.68182	30.68182	18.5446	36.2676	47.30047	55.96855	9.59878	20.73171	27.7439	37.19512	41.07143	64.28571	69.64286	74.10714	79.10798	84.14834	89.17602	41.07143	64.28571	69.64286	74.10714	79.10798	84.14834	89.17602	100
		trial3	9.09091	22.72727	30.68182	35.27272	16.66667	30.86855	38.7324	46.94836	10.92317	24.2378	34.7961	43.44512	41.96429	61.60714	68.75	77.67857	84.14834	89.17602	94.07362	41.96429	61.60714	68.75	77.67857	84.14834	89.17602	100	100
		avg	12.87979	24.02121	31.43939	34.4697	17.60583	34.74178	44.99218	53.16902	9.998337	22.71341	31.09756	39.76658	41.07143	61.90476	69.64286	77.08333	84.14834	89.17602	94.07362	41.07143	61.90476	69.64286	77.08333	84.14834	89.17602	100	100
		std	3.471647	2.365532	1.312156	3.471647	0.938985	3.37938	5.48303	5.402886	0.896631	1.797226	3.516028	3.258774	0.89286	2.246972	0.892855	2.727727	2.727727	2.727727	2.727727	0.89286	2.246972	0.892855	2.727727	2.727727	2.727727	2.727727	2.727727
UMA	CA	trial1	40.69767	66.27907	79.06977	84.88372	23.7927	47.34982	59.71732	73.38045	29.09484	50.38285	61.8683	69.67841	66.36364	94.54546	98.18182	100	100	100	100	66.36364	94.54546	98.18182	100	100	100	100	100
		trial2	38.37209	60.46511	70.93023	80.23256	27.79741	52.61255	65.01767	75.02945	30.62787	56.43645	65.3905	71.97549	79.09091	94.54546	100	100	100	100	79.09091	94.54546	100	100	100	100	100	100	100
		trial3	48.83721	75.5814	86.04651	93.02225	21.90813	43.4629	59.95288	68.55124	28.17764	49.31087	62.17458	71.05686	64.54546	89.09091	94.54546	96.36364	96.36364	96.36364	96.36364	64.54546	89.09091	94.54546	96.36364	96.36364	96.36364	96.36364	96.36364
		avg	42.63566	67.44186	76.68217	86.04651	24.49941	47.62468	61.56262	72.32038	29.30068	51.71006	62.17458	71.05686	70.90909	94.54546	98.18182	100	100	100	100	70.90909	94.54546	98.18182	100	100	100	100	100
		std	5.495137	7.624834	7.565559	6.474141	3.007572	4.305769	2.994475	3.969692	1.237811	3.271359	1.951147	1.156172	7.925269	3.149186	2.777316	2.09453	2.09453	2.09453	2.09453	7.925269	3.149186	2.777316	2.09453	2.09453	2.09453	2.09453	2.09453
UMA	C3T	trial1	59.09091	86.63636	96.59091	96.59091	33.21596	59.39947	70.77465	77.93427	49.08537	70.04878	83.84146	88.41463	81.25	97.32143	99.10714	99.10714	100	100	100	81.25	97.32143	99.10714	99.10714	100	100	100	100
		trial2	60.22727	84.09091	92.04546	94.31818	32.277	58.4507	70.77465	77.93427	51.21951	70.96342	84.60366	88.87195	86.17857	96.42857	99.10714	99.10714	100	100	100	86.17857	96.42857	99.10714	99.10714	100	100	100	100
		trial3	68.18182	86.36364	90.90909	95.45454	31.68014	55.8592	66.90141	72.65258	53.33366	73.2683	85.3685	88.87195	86.17857	96.42857	99.10714	99.10714	100	100	100	86.17857	96.42857	99.10714	99.10714	100	100	100	100
		avg	62.5	86.36364	93.18182	95.45454	32.94337	57.9421	69.40532	76.06534	51.21951	70.77465	84.60366	88.87195	86.17857	96.42857	99.10714	99.10714	100	100	100	86.17857	96.42857	99.10714	99.10714	100	100	100	100
		std	4.953296	2.272725	3.006535	1.136365	0.769651	1.7795	2.171627	2.922993	2.134145	0.634658	0.762106	0.264034	5.154912	0.515483	0.515483	0.515483	0.515483	0.515483	0.515483	5.154912	0.515483	0.515483	0.515483	0.515483	0.515483	0.515483	0.515483

Figure 11: **Full results:** across all trials for Table 1. Values that we used in Table 1 are highlighted and the best performance of each method within supervised and UMA are bolded.

In this appendix, we first discuss related studies and directions 7.1, then provide additional additional visualizations given above and summarize them in Section 7.2. Then, we discuss the limitations and future direction of this work. Further, we provide additional experiments in Section 7.4, additional ablations in Section 7.5, and further details on our methods in Section 7.6. Finally, we provide details on each of the datasets used in Section 7.7 and explore additional baselines to compare our methods to in Section 7.8.

7.1 Related Works

Unsupervised Modality Adaptation In domain adaptation, a model trained in a source domain is tasked with efficiently adapting to a related target domain that contains fewer labeled data points [31, 32]. Given the focus on domains with scarce labels, adaptation is often achieved through unsupervised [12] or semi-supervised [6] methods. In the context of IMU-based HAR [13], domain adaptation may involve adapting between different sensors [33], adjusting to varying positions of wearables on the body [34, 12, 35], accommodating different users [36, 37], or adapting to different IMU device types [38–40]. Our work focuses on unsupervised domain adaptation where the target domain is a new, completely unlabeled modality. Hence, we introduce the term Unsupervised Modality Adaptation (UMA). Other research works explore similar concepts, such as knowledge distillation, missing modality, robust sensor fusion, multimodal alignment; however, most of these works require *some* labels from the target modality in training to update the model, thus do not work in UMA [8–11]. We use the term UMA to discuss performing test-time inference when *zero* labeled instances of the target modality are available during training.

Student-Teacher: Student-teacher methods involve two distinct models: a teacher (source) model that imparts knowledge to a student (target) model during the training process. Knowledge distillation methods often employ an extra auxiliary modality as the teacher during training to increase the student modality’s performance during testing; however, they assume the availability of labeled training data from both modalities [15, 16, 9, 17]. In particular, Thoker and Gall [14] perform knowledge distillation without labels for the student modality data during training consistent with the UMA framework. Thus, their method is used as our student teacher baseline (ST). Nevertheless, their work is tested on one RGB+D dataset and lacks noise experiments, latent visuals, and comparisons to similar methods.

In addition, IMUTube [41] and ChromoSim [42] simulate IMU data from videos to train an IMU model. In this instance, the teacher is the simulator, which trains the student IMU model without using any real IMU data. However, these approaches are resource-intensive, cannot easily extend to other modalities, and face simulation-reality gaps.

Contrastive Alignment: Unsupervised contrastive alignment methods for IMU data include IMU2CLIP [1], ImageBind [2], and mmg-Ego4d [3]. While these approaches have shown promise in retrieval and generation tasks, they have limitations. All these methods focus exclusively on egocentric data. IMU2CLIP [1] aligns IMU data with text labels which violates the UMA setting. ImageBind [2] is not well tested with IMU data, is computationally intensive, and is not explicitly tested in the UMA setting. Mmg-Ego4d [3] addresses UMA with their zero-shot cross-modal transfer task, but their work is limited to a single private ego-centric dataset and focuses mainly on few-shot label learning. We use mmg-Ego4d as our CA baseline and run extensive UMA experiments, encompassing both egocentric and third-person camera-view public datasets Table 1. We further test its robustness to temporal distortions Table 2, its ability to scale with the latent vector size Figure 3, and we visualize its multimodal latent space Figure 5.

Cross-modal Transfer Through Time: Existing video understanding and robust sensor fusion methods often leverage temporal data, employing techniques such as temporal masking and reconstruction [43, 16], spatio-temporal memory banks [44], or fusion of temporal chunks through transformer self-attention [45–47]. However, these approaches typically assume the availability of labeled data for all modalities in a specific task, limiting their applicability to the UMA setting. Unlike traditional methods inspired by ViT [48] and SwinTransformers [49], which chunk data into fixed or shifted time segments, C3T learns temporal tokens through temporal convolutions and uses them as a multi-vector latent space to align time-series modalities for cross-modal transfer.

7.2 Visualizations

Figure 6 is an expanded version of Figure 5 to show the points more clearly. Figure 7 visualizes the C3T latent space and a shifted input into that latent space. Figure 8 visualizes the C3T latent space with a shifted input and its original input. Figure 9 visualizes the CA latent space on a different dataset, CZU-MHAD. Figure 10 shows another visualization of the progression of the latent space in CA through training.

7.3 Limitations and Future Directions:

Our novel visualizations of a joint multimodal latent space leave much room for future exploration. For example, in Figure 5 IMU data points consistently cluster towards the center of the plot, with RGB points surrounding them (more examples in Section 7.2). The consistency of this pattern suggests that the latent space may not be completely modality-agnostic. This phenomenon is an interesting direction for future research, potentially offering additional insights into cross-modal representations.

Furthermore, C3T’s architecture has room to scale to larger models and backbones and test on other types of data. Given our theoretical intuition that alignment across local features is beneficial, and our time-shift visualizations in Figure 4 we believe C3T’s method would generalize to other types of data or transfer scenarios involving time-series modalities.

We hypothesize C3T can easily extend to various tasks as well. Our training experiments in Section 5 show that C3T performs best by aligning the modalities first and our latent visualization in Figure 5 show structure in the multimodal latent space before labels are introduced. This suggest that our architecture may actually be able to transfer easily to various tasks. For example, after the alignment phase has been performed once, adding an additional task should only require training an additional task-specific head. We hypothesize that without additional alignment, we may be able to train a person identification task head-on the IMU latent representations and then perform person identification with the RGB images without ever needing additional RGB data. This sort of multi-task transfer investigation would be a valuable future extension of this work.

Discussion of potential positive and negative impacts of the work: As stated in the introduction, cross-modal transfer for sensor data has numerous positive applications, in healthcare, smart homes, smart devices, user interface design etc. Some negative impacts that may occur are that social bias may transfer across modalities, certain modalities might not be accessible to individuals with disabilities, exacerbating the technology gap between the able-bodied and disabled, and cross-modal transfer may increase certain security and privacy concerns if someone’s identity/information can easily be transferred across modalities.

7.4 Additional Experiments

Extended: Can UMA methods retain performance on the labeled modality? Can they leverage both modalities?

Experimental setup: Table 5 shows the result of training in the UMA setting but testing with all combinations of the modalities. Any inputs can be used to perform HAR by simply using the HAR module h on an estimate for the latent vector, \hat{z} derived from the modalities. For ST, h can be viewed as the identity, and z ’s are the output logits.

1. **RGB (Supervised Learning):** Tests the model on RGB data, which was labeled during training, thus this is supervised paradigm. The estimated latent vector is given by $f^{(1)}(x_i^{(1)}) = \hat{z}_i$.
2. **IMU (UMA):** Is the main result of this paper and described above in Section 3. Here the estimated latent vector is given by $f^{(2)}(x_i^{(2)}) = \hat{z}_i$.
3. **Both (Sensor Fusion):** Merges latent vectors from each modality. Assuming each estimate is equally as good as the other: $\hat{z}_i = \mathbb{E}[z_i | x_i^{(1)}, x_i^{(2)}] = E[z_i | \hat{z}_i^{(1)}, \hat{z}_i^{(2)}] = \frac{\hat{z}_i^{(1)} + \hat{z}_i^{(2)}}{|\hat{z}_i^{(1)} + \hat{z}_i^{(2)}|}$. Given that we align the latent vectors from different modalities by minimizing the angle between them, i.e. cosine similarity, we also fuse vectors by generating the normalized vector whose angle is halfway between the estimated vectors.

Results: As expected, Table 5 shows that C3T outperforms the other methods. When comparing the performances in the different test scenarios, our experiments indicate that when given both modalities,

fusion performs better than the RGB model alone. Instead of introducing noise or uncertainty into the model, introducing an unlabeled modality may add structure to the shared latent space that bolsters performance, especially if that modality is highly informative for the given task. This observation bears resemblance to knowledge distillation methods, where an auxiliary modality during training leads to improved testing outcomes, however, these methods usually assume that auxiliary modality is labeled [30]. The application of UMA to sensor fusion presents a promising avenue for future research.

Additional Dataset: We revisited this question of testing on different modalities from the main paper and attempted to test on other modalities for different datasets. We noticed that the results were consistent with our main findings, that often testing with both modalities performs better than testing with the training modality that had labels (RGB)! See Table 6 below for the results on the MMACT dataset.

Table 6: **UMA Testing on Each Modality** Accuracy MMACT [16] when trained for UMA and tested on only RGB data, only IMU data, or Both.

Model	1. RGB	2. IMU	3. Both
ST	25.8%	16.7%	25.8%
CA	39.9%	26.9%	41.3%
C3T	39.2%	31.7%	47.3%

How quickly can our models learn from labeled IMU samples?

As illustrated in Figure 12, CA demonstrates faster learning, reaching peak performance within 20 shots, while C3T requires about 40 shots. Neither method matches the supervised IMU performance of 87.9% reported in Table 1, but they approach the fusion performance of approximately 62%.

It’s important to note that this comparison with the supervised baselines may not be entirely fair, as the supervised baselines had access to the entire Train HAR dataset (40% of the data), whereas, the few-shot learning was conducted on the validation set (10% of the data). Given that the supervised IMU and fusion models share the same architecture as CA, repurposed for the supervised setting, we would expect similar performance under equal conditions.

Nonetheless, these experiments clearly demonstrate CA’s superior ability in few-shot cross-modal learning compared to C3T. As shown in Figure 12, both IMU and combined modality performance improve with increasing shots, while RGB performance remains constant due to the learning shots containing only labeled IMU data.

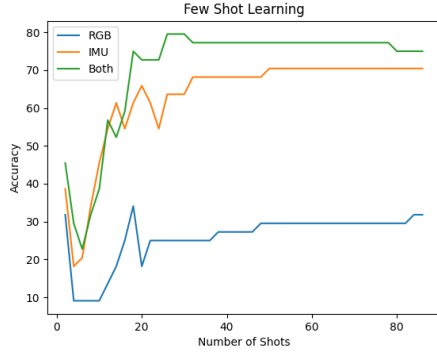
7.5 Additional Ablations:

We conducted a brief ablation study on the alignment loss, comparing our cosine similarity approach with the conventional L2 loss. As shown in Table 7, the results strongly support our initial intuition presented in Section 2. The substantial performance gap between cosine similarity and L2 loss for both CA and C3T models underscores that cosine similarity is indeed a more effective measure of alignment for high-dimensional vectors in this context. These findings align with well-established principles in high-dimensional space analysis, reinforcing the validity of our approach. Given the well-established nature of these results, we have included this comparison in the supplementary material rather than the main paper, focusing the primary discussion on novel contributions.

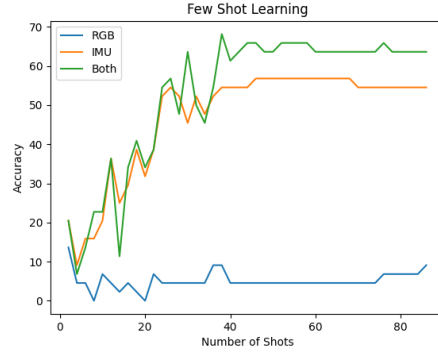
Table 7: **Alignment Loss Comparison:** Performance of CA and C3T models using Cosine Similarity and L2 loss for alignment on the UTD-MHAD dataset.

Model	Cosine Similarity	L2 Loss
CA	44.32	2.27
C3T	62.50	3.41

Lastly, we provide an extension of our architecture ablations in Table 8. In this extension, we also ablate the encoders of the supervised baselines, which are the same modules used for ST, CA and C3T, however, trained in the supervised setting, as opposed to UMA. The only interesting result is



(i) CA Cross-Modal Few Shot



(ii) C3T Cross-Modal Few Shot

Figure 12: **Cross-Modal Few Shot Learning Comparison:** (a) CA method and (b) C3T method performance in cross-modal few shot learning scenarios when testing on IMU, RGB and Both modalities. RGB performance remains the same because the learning shots only contain labeled IMU data. However, we can see IMU and Both performance rise.

that the RGB baseline may have performed better with an attention-based temporal feature extractor. This could potentially imply that the C3T does not surpass the best supervised RGB model, as we noted in the main results. It is not necessary to ablate the unimodal supervised setting because that is not the main novel method of this work. We believe there exist other Video Action recognition models that are better. However, this does not contradict the main findings of this paper that C3T is the most robust to temporal noise in the UMA cross-modal transfer setting.

7.6 Methods:

Table 9 shows the data splits used for Unsupervised Modality Adaptation (UMA) training. All tables report the accuracy on the \mathcal{D}_{Test} for each method ($\text{accuracy} = \frac{1}{I_4} \sum_{i=1}^{I_4} \mathbb{1}_{\hat{y}_i = y_i}$).

For reproducibility and to guarantee the scientific rigor of our experiments, our main results table in Table 1 was run 3 times with random seeds pytorch 1,2 and 3. The full results are given in Figure 11. The results report the average values across all trials and their standard deviations across those 3 trials. We note, that although the standard deviations are quite large, the difference in performance between the methods is typically larger than one standard deviation, implying statistical significance in our comparative analysis. This suggests that the observed performance improvements of C3T over baseline methods are not merely due to random variation but represent genuine algorithmic advantages. Furthermore, the consistent pattern of outperformance across multiple datasets strengthens the reliability of our conclusions, as the probability of observing such consistent results by chance across independent experiments would be exceedingly low. We also note that the supervised methods were only trained on 40% of the data given in \mathcal{D}_{HAR} for a fair comparison to the other methods.

Datasets and Hyperparameters - Additional Info: We present results on four diverse datasets: (1) UTD-MHAD [19], a small yet structured dataset; (2) CZU-MHAD [20], a slightly larger dataset captured in a controlled environment; (3) MMACT [16], a very large dataset with various challenges including different view-angles, scenes, and occlusions; and (4) MMEA-CL [21], an egocentric camera dataset. For each dataset, we create an approximately 40-40-10-10 percent data split for the \mathcal{D}_{Align} , \mathcal{D}_{HAR} , \mathcal{D}_{Val} , and \mathcal{D}_{Test} sets respectively, as shown in Appendix Table 9. \mathcal{D}_{Val} was used to perform a minor hyperparameter search on the UTD-MHAD dataset. The methods performed best with a learning rate of 1.5×10^{-4} , a batch size of 16, num_workers of 4, and a latent representation dimension of 2048 with an Adam optimizer. The preprocessing steps downsample the video to $t = 30$ frames, and C3T extracts $t_{fm} = 15$ latent vectors per sample. Experiments were implemented in Pytorch and run on a 16GB NVIDIA Quadro RTX 5000, four 48GB A40s, or four 48GB A100s and

Table 8: **Architecture Ablation Extensions:** This shows an extension of our architecture ablations (Table 3) to baselines. It shows a comparison of different architectures for RGB and IMU encoders across various methods. We report encoder types for spatial and temporal dimensions of RGB data, and the temporal dimension for IMU data, along with the number of parameters (in millions) and accuracy for each configuration. Convolutional architectures generally yielded superior performance, while still maintaining a relatively low model size. These results indicate that C3T’s performance advantage stems from its methodological approach rather than solely from its attention head or size.

Method	RGB		IMU	Params (M)	Accuracy (%)
	Spatial	Temporal	Temporal		
ST	Conv	Conv	Conv	129.2	12.9
	Conv	Conv	Attn	97.8	10.2
	Conv	Attn	Conv	871.2	11.4
	Attn	Conv	Conv	291.5	5.7
CA	Conv	Conv	Conv	163.8	38.6
	Conv	Conv	Attn	132.3	19.3
	Conv	Attn	Conv	905.7	34.1
	Attn	Conv	Conv	326.0	26.1
C3T	Conv	Conv	Conv	137.7	62.5
	Conv	Conv	Attn	106.3	15.9
	Conv	Attn	Conv	879.6	53.4
	Attn	Conv	Conv	300.0	33.0
FUSION	Conv	Conv	Conv	163.8	62.5
	Conv	Conv	Attn	132.3	77.3
	Conv	Attn	Conv	905.7	89.8
	Attn	Conv	Conv	326.0	64.8
IMU	–	–	Conv	32.0	87.9
	–	–	Attn	0.5	27.3
RGB	Conv	Conv	–	97.3	53.8
	Conv	Attn	–	839.2	71.6
	Attn	Conv	–	259.5	64.8

Table 9: **Data Splits for Unsupervised Modality Adaptation (UMA):** During training, no labeled IMU data is present, thus the model can only leverage the correlations between X^{IMU} and X^{RGB} to learn classes for IMU data.

Split	X^{RGB}	X^{IMU}	Y	% of Data
\mathcal{D}_{HAR} : Train a)	✓		✓	40%
$\mathcal{D}_{\text{Align}}$: Train b)	✓	✓		40%
\mathcal{D}_{Val} : Val		✓	✓	10%
$\mathcal{D}_{\text{Test}}$: Test		✓	✓	10%

each run took between 4-10 hours, depending on the dataset and GPU availability. More detailed information about each dataset and implementation can be found in Appendix Section 7.7.

Main Table With All Train Method 1: Before the ablations discovered that Train method 4 (combined loss) was better for CA we used method 1 (Align first). Table 10 shows the original experiments with all UMA models trained using method 1 (align first) and we observe no difference in the resulting rankings of the method.

Student Teacher: Below is the standard cross-entropy loss that was employed for the student teacher methods.

$$\mathcal{L}_{CE}(P_{\hat{y}}, P_y) = -\frac{1}{N} \sum_{i=1}^N \sum_{j=1}^C \mathbb{1}_{y_i=j} \log\left(\frac{\exp \hat{y}_{i,j}}{\sum_{i=1}^M \exp \hat{y}_{i,j}}\right) \quad (3)$$

where \hat{y}_i is the output of the i th sample in the batch of N samples, $\hat{y}_{i,j}$ is the score for the j th class out of C classes, and P_y represents the probability distribution produced by a given model’s output logits.

Table 10: **UMA performance compared to supervised baselines Using Train Method 1:** Each method is modular and can be decomposed to perform in the traditional supervised setting, or can be combined into ST, CA or CT3 to perform UMA. We developed all models from scratch, however, ST and CA resemble existing methods whereas C3T introduces novel mechanisms. Top-1 and Top-3 accuracies are reported for each dataset. Although ST performs poorly, it performs significantly better than randomly guessing, indicating it is still learning action information from the RGB data without any labels. Please note the CA row of this table reports the results when trained using training method 1 (align first). The overall does not differ from Table 1 indicating that the performance results of C3T are not biased by the training method.

	Model	UTD-MHAD		CZU-MHAD		MMACT		MMEA-CL	
		Top-1	Top-3	Top-1	Top-3	Top-1	Top-3	Top-1	Top-3
Supervised	IMU	87.9	97.7	95.1	98.2	70.0	90.0	65.8	87.6
	RGB	53.8	73.1	94.0	99.7	42.1	61.6	54.2	77.1
	Fusion	62.5	82.2	95.0	98.5	76.7	92.0	80.1	92.7
UMA	Random	3.7	11.1	4.6	16.6	2.9	8.6	3.1	9.4
	ST	12.9	24.6	41.1	61.9	17.6	34.7	9.9	22.7
	CA	38.6	56.1	81.0	95.5	27.3	45.6	42.3	62.1
	C3T	62.5	86.4	84.2	96.7	32.4	57.9	51.2	78.8

The teacher network minimizes $\mathcal{L}_{CE}(P_{f^1(x)}, P_y)$ and the student minimizes $\mathcal{L}_{CE}(P_{f^2(x)}, P_{f^2(x)})$. Since the student approximates the teacher and the teacher approximates the true distribution, this implies that the student can only be as good as the teacher at approximating the true distribution:

$$\mathcal{L}_{CE}(P_{f^1(x)}, P_y) \leq \mathcal{L}_{CE}(P_{f^2(x)}, P_y) \quad (4)$$

C3T Modules Here we provide a more precise formulation of the modules used for C3T.

The updated modules are as follows:

Video Feature Encoder $f^{(1)} : \mathcal{X}^{(1)} \rightarrow \mathcal{Z}^{t_{rec}}$: This module applies a pretrained Resnet18 to every frame a video and then performs a single 3D convolution. The resulting output is a set t_{rec} z : $\hat{\mathbf{Z}}^{(1)} = (\hat{z}_1^{(1)} \dots \hat{z}_{t_{rec}}^{(1)})$.

IMU Feature Encoder $f^{(2)} : \mathcal{X}^{(2)} \rightarrow \mathcal{Z}^{t_{rec}}$: This is a 1D CNN that decreases the time dimension to t_{rec} , resulting in an output of $\hat{\mathbf{Z}}^{(2)} = (\hat{z}_1^{(2)} \dots \hat{z}_{t_{rec}}^{(2)})$.

HAR Task Decoder $h : \mathcal{Z}^{t_{rec}} \rightarrow \mathcal{Y}$: This module is like a transformer encoder that uses self-attention on an input sequence of length t_{rec} vectors appended with a learned class token. The output class token of the self attention layer is then passed through a FFN and outputs a single action label y_i .

7.7 Datasets

Here we provide more information on the datasets and how they were used in our experiments.

UTD-MHAD Most of the development and experiments were performed on the UTD-Multi-modal Human Action Dataset (UTD-MHAD) [19]. This dataset consists of roughly 861 sequences of RGB, skeletal, depth and an inertial sensor, with 27 different labeled action classes performed by 8 subjects 4 times. The inertial sensor provided 3-axis acceleration and 3-axis gyroscopic information, and all 6 channels were used for in our model as the IMU input. Given our motivation, we only use the video and inertial data; however, CA can easily be extended to multiple modalities.

CZU-MHAD The Changzhhou MHAD [20] dataset provides about 1,170 sequences and includes depth information from a Kinect camera synchronized with 10 IMU sensors, each 6 channels, in a very controlled setting with a user directly facing the camera for 22 actions. They do not provide RGB information, thus we use depth as the visual modality, broadcast it to 3 channels, and pass it into the RGB module. We concatenate the IMU data to provide a 60-channel input as the IMU modality and use depth as the input modality. Given the controlled environment and dense IMU streams, the models performed the best on this dataset.

MMACT The MMACT dataset [16] is a large scale dataset containing about 1,900 sequences of 35 action classes from 40 subjects on 7 modalities. This data is challenging because it provides data from 5 different scenes, including sitting at a desk, or performing an action that is partially occluded by

an object. Furthermore, the data was collected with the user facing random angles at random times. The dataset contains 4 different cameras at 4 corners of the room, and it measures acceleration on the user’s watch and acceleration, gyroscope and orientation data from a user’s phone in their pocket. We only use the cross-view camera 1 data, and again we concatenate the four 3-axis inertial sensors into one 12-channel IMU modality.

MMEA-CL The Multi-Modal Egocentric Activity recognition dataset for Continual Learning (MMEA-CL) [21] is a recent dataset motivated by learning strong visual-IMU based representations that can be used for continual learning. It provides about 6,4000 samples of synchronized first-person video clips and 6-channel accelerometer and gyroscope data from a wrist worn IMU for 32 classes. The dataset’s labels feature realistic daily actions in the wild, as opposed to recorded sequences in a lab. Due to issues with the data and technical constraints, we downsize the data proportionally from each class and use about the first 1,000 samples. However, CT3’s superior performance shows how this method can generalize to a camera view (ego-centric camera), and different types of activities.

7.8 Baselines

This method attempts to adapt existing methods to UMA and compare them as baselines against our methods.

Many works deal with robustness to missing sensor data during training or testing, however, few works deal with zero-labeled training data from one modality. As a result, constructing baselines is tricky and most methods had to be modified or adapted to fit our approach. Even so, as shown in Table 11 These methods perform very poorly in the UMA setting.

We would like to note that all the baselines and methods were trained and tested on the same data splits, i.e. it’s not the case that they have different train a) and train b) splits. We believe that this allows for fair comparison. In addition, the supervised baselines were only trained on the Train a) Supervised HAR split. This ensures that the supervised baselines do not have an unfair advantage of seeing more data (they also only see 40% of the labeled data not 80%). The exact data splits are also provided in a separate repository linked in our code.

7.8.1 Sensor Fusion Baselines

Sensor fusion is often broken down into the following 3 methods based on where the data are combined [50–52], also shown in Figure 13:

1. Early or data-level fusion combines the raw sensor outputs before any processing.
2. Middle/intermediate or feature-level fusion combines each sensor modality after some preprocessing or feature extraction.
3. Late or decision-level fusion combines the raw output, essentially ensembling separate models.

Many IMU-RGB based sensor fusion models have the ability to train on partially available or corrupted data and are robust to missing modalities during inference [44, 53]. Sensor fusion works rarely attempt the extreme case where one modality is completely unlabeled during training. Existing sensor fusion methods can be adapted to our setup using a psuedo- labeling technique, similar to the student-teacher model above. The difference for sensor fusion is that the model learns a joint distribution between the two modalities as opposed to two separate distributions. Thus the model may be able to learn some correlation between the modalities. Nonetheless, we show that these methods cannot generalize to the scenario where there is zero-labeled training data for one modality.

Let $g(\cdot, \cdot) : (\mathcal{X}^{(1)}, \mathcal{X}^{(2)}) \rightarrow \mathcal{Y}$. Our approach uses \mathcal{D}_{HAR} , to train by passing in zeros for one modality, e.g. we train $g(\cdot, \mathbf{0}) : \mathcal{X}^{(1)} \rightarrow \mathcal{Y}$. Then, with \mathcal{D}_{Align} we use $g(\cdot, \mathbf{0})$ to generated psuedo-labels and then train $g(\mathbf{0}, \cdot, \cdot)$ with those labels.

We reproduced the conventional sensor fusion models (early, feature, and late) from [54] and indicate the performance of the top model on 11. We further reproduce a self-attention based sensor fusion approach (HAMLET [53]) and tested it on our setup. We follow a very similar architecture; however, extract spatio-temporal results using 3D convolution in the video as opposed to an LSTM. This method provides similar results as the LSTM method on the standard sensor fusion problem. To verify the integrity of our reproduced models we compared to state-of-the-art reported methods and showed similar performance results. The results are given in Table 12. We selected HAMLET due to its state-of-the-art performance on the UTD-MHAD dataset, making it

Table 11: **UMA with Existing Methods:** Most methods fail to adapt to zero-shot cross-modal transfer from the RGB to IMU sensor modalities. Imagebind performs well on MMEA, which is an egocentric dataset, similar to Ego-4d in which Imagebind was trained on.

Model	UTD-MHAD	MMACT	MMEA- CL	CZU-MHAD
Sensor Fusion (2019) [54]	5.2%	3.2 %	4.1 %	4.5 %
HAMLET (2020) [53]	4.6 %	3.2 %	4.1 %	4.5 %
ImageBind (2023) [2]	11.3 %	4.6 %	40.1 %	4.54 %
Student Teacher	12.9 %	17.6 %	9.9 %	41.1%
Contrastive Alignment	38.6 %	27.3 %	42.3 %	81.0 %
Cross-modal Transfer Through Time (Ours)	62.5 %	32.4 %	51.2 %	84.2 %

an ideal benchmarks for comparison with our model. These experiments prove that our reproduced baselines are comparable to SOTA method. In addition, these baselines fail to perform well in the UMA setting underscoring the importance and novelty of our work.

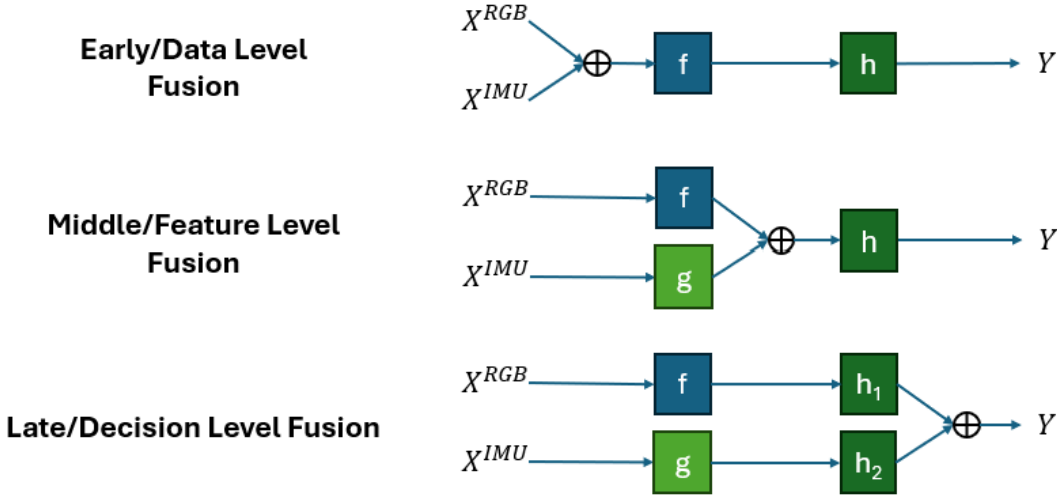


Figure 13: Types of Sensor Fusion

Table 12: SOTA Sensor Fusion Performance on UTD-MHAD. † [54], * [53]

REPORTED MODELS	ACCURACY
HAMLET *	95.12%
WEI ET AL. †	95.6%
REPRODUCED FROM †	ACCURACY
EARLY FUSION	86.71%
FEATURE FUSION	95.60%
LATE FUSION	94.22%

7.8.2 Contrastive Learning Baseline

ImageBind [2] learns encoders for 6 modalities, (Images/Videos, Text, Audio, Depth, Thermal and IMU) by performing CLIP’s training method [18] between each of those encoders and the Image/Video encoder. It was well tested for image, text and audio-based alignment, retrieval, and latent space generation tasks, however was not well tested with IMU data and not used for specific tasks, such as HAR. In addition, one fundamental difference between Imagebind and CA is that Imagebind constructs a latent space amongst the sensing modalities and text and aligns between them. We hypothesize that this vector space is more difficult and unnecessary to construct, for human action recognition using sensing modalities. The text modality, although sequential in nature, does not have a time dimension, thus it cannot leverage correlations between modalities in time like

C3T. We work with the original Imagebind model and code released on github ¹. We perform two conventional task-specific adaptations for CLIP models: Zero Shot transfer and Linear Probing:

Zero-Shot Transfer: Let's denote the video, IMU and text encoders as $g^{(1)} : \mathcal{X}^{(1)} \rightarrow \mathcal{Z}$, $g^{(2)} : \mathcal{X}^{(2)} \rightarrow \mathcal{Z}$, and $g^{(3)} : \mathcal{X}^{(3)} \rightarrow \mathcal{Z}$ respectively. First, we attempt zero-shot transfer. Here, we pass all the action labels through the text encoder of the pretrained model. For a dataset with C classes, we have $\hat{Z}^{(3)} = (\hat{z}_1^{(3)} \dots \hat{z}_C^{(3)})$. Finally, for a given IMU sample $(x_i^{(2)}, y_i) \in \mathcal{D}_{Test}$, we pass $x_i^{(2)}$ through the IMU encoder $g^{(2)}$ and retrieve $\hat{z}^{(2)}$. Then, we classify the point by looking at which points gives the highest cosine similarity score in the latent space, e.g. $\hat{y}_i = \underset{j}{argmax} \frac{\langle x_i^{(2)}, \hat{z}_j^{(3)} \rangle}{||\langle x_i^{(2)}, \hat{z}_j^{(3)} \rangle||}$. The video encoder $g^{(1)}$ goes unused as no training was done, and in UMA, there is no video data during testing. This performed poorly and the results are not reported.

Linear Probing: Given that ImageBind is a large model trained on massive corpuses of data it becomes impractical to train the model from scratch on our smaller datasets collected from wearables and edge devices. Instead, we fine-tuned the ImageBind model using a linear projection head on the encoders, that can then be trained for a specific task. The results of this method are depicted in Table 11.

The results show a poor generalization of Imagebind to most experiments on our setup, and we hypothesize a few reasons. Firstly, ImageBind is a large model and may either overfit to small datasets, or not have enough training examples to learn strong enough representations. Second, ImageBind was pre-trained on Ego4D and Aria which contain egocentric videos to align noisy captions with the IMU data, whereas our datasets had fixed labels and were mostly 3rd person perspective. In fact ImageBind performed the best on the one egocentric dataset we used, MMEA-CL[21]. Lastly, Imagebind was trained on a IMU sequences of 10s length sampled at a much higher frequency, thus we zero-padded or upsampled the IMU data to fit into ImageBind's IMU encoder, and the sparse or repetitive signal may have been too weak for ImageBind's encoder to accurately interpret the data.

¹<https://github.com/facebookresearch/ImageBind>